Diatom resting spore ecology drives enhanced carbon export from a naturally iron-fertilized bloom in the Southern Ocean

Ian Salter, Alan E. S. Kemp, C. Mark Moore, Richard S. Lampitt, George A. Wolff, Jens Holtvoeth

Diatom resting spore ecology drives enhanced carbon export from a naturally iron-fertilized bloom in the Southern Ocean

Ian Salter,[1,2] Alan E. S. Kemp,[1] C. Mark Moore,[1] Richard S. Lampitt,[1] George A. Wolff,[3] and Jens Holtvoeth[3]

Received 28 October 2010; revised 20 October 2011; accepted 25 October 2011; published 1 February 2012.

[1] Southern Ocean Island systems sustain phytoplankton blooms induced by natural iron fertilization that are important for the uptake of atmospheric carbon dioxide and serve as analogues for past and future climate change. We present data on diatom flux assemblages and the biogeochemical properties of sinking particles to explain the enhanced particulate organic carbon (POC) export fluxes observed in response to natural iron supply in the Crozet Islands region (CROZeX). Moored deep-ocean sediment traps (>2000 m) were located beneath a naturally fertilized island bloom and beneath an adjacent High Nutrient Low Chlorophyll (HNLC) control site. Deep-ocean carbon flux from the naturally-fertilized bloom area was tightly correlated ($R = 0.83$, $n = 12$, $P < 0.0006$) with the resting spore flux of a single island-associated diatom species, *Eucampia antarctica* var. *antarctica*. The unusually well preserved state of the *Eucampia*-associated carbon flux, determined by amino acid studies of organic matter degradation, was likely influenced by their ecology, since diatom resting spores are adapted to settle rapidly out of the surface ocean preserving viable cells. The naturally fertilized bloom enhanced carbon flux and the resulting Si/C and Si/N ratios were 2.0–3.4-fold and 2.2–3.5-fold lower than those measured in the adjacent HNLC control area. The enhanced carbon export and distinctive stoichiometry observed in naturally fertilized systems is therefore largely not attributable to iron relief of open ocean diatoms, but rather to the advection and growth of diatom species characteristic of island systems and the subsequent flux of resting spores. Carbon export estimates from current natural iron fertilization studies therefore represent a highly specific response of the island systems chosen as natural laboratories and may not be appropriate analogues for the larger Southern Ocean response. The broader implications of our results emphasize the role of phytoplankton diversity and ecology and highlight the need for a species-centered approach in order to understand the regulation of biogeochemical fluxes.

Citation: Salter, I., A. E. S. Kemp, C. M. Moore, R. S. Lampitt, G. A. Wolff, and J. Holtvoeth (2012), Diatom resting spore ecology drives enhanced carbon export from a naturally iron-fertilized bloom in the Southern Ocean, *Global Biogeochem. Cycles*, *26*, GB1014, doi:10.1029/2010GB003977.

1. Introduction

[2] The Southern Ocean is regarded as a critical player in the global carbon cycle through the ability of changes in its circulation to affect ocean ventilation and sensitivity of atmospheric CO_2 drawdown to its level of nutrient depletion [*Marinov et al.*, 2008a, 2008b; *Takahashi et al.*, 2002]. The biological draw-down of atmospheric CO_2 is not only controlled by the amount of production but the extent to which the carbon fixed by phytoplankton is exported out of the surface ocean and beyond the ventilation depth. Despite sufficient concentrations of macronutrients, primary production in the Southern Ocean is limited, resulting in its high nutrient low chlorophyll (HNLC) status. The strength (and efficiency) of the biological carbon pump is sub-optimal under HNLC conditions.

[3] Following the advent of the iron hypothesis [*Martin*, 1990], numerous *in situ* iron-fertilization studies have demonstrated that the addition of iron to Southern Ocean HNLC waters stimulates phytoplankton production [*Boyd et al.*, 2000; *Coale et al.*, 2004; *Hoffmann et al.*, 2006]. Although some artificial iron fertilization experiments have indicated enhanced carbon flux from the surface ocean [*Buesseler et al.*, 2005], others have not [*Nodder et al.*, 2001]. This inconsistency may be attributed in part to the relatively short

[1]National Oceanography Centre, Southampton, University of Southampton, Southampton, UK.
[2]Laboratoire d'Océanographie Microbienne, Observatoire du Banyuls-sur-mer, Université Pierre et Marie Curie, CNRS-INSU-UMR 7621, Banyuls-sur-mer, France.
[3]Department of Earth and Ocean Sciences, University of Liverpool, Liverpool, UK.

0886-6236/12/2010GB003977

time scales and limited spatial scales of artificial fertilization experiments that have confounded reliable estimates of export [*Boyd et al.*, 2000], but could also relate to the phytoplankton species involved, since some taxa may export carbon more effectively than others [*Smetacek et al.*, 2004].

[4] In contrast to the discrete pulses of iron characteristic of artificial iron enrichment experiments, the recurrent phytoplankton blooms around Southern Ocean island systems [*Moore and Abbott*, 2002] are fertilized by natural sources of iron and receive a prolonged regular, although seasonal input, so that observational limitations may be more readily overcome [*Boyd et al.*, 2000]. Natural fertilization experiments undertaken around the Kerguelen [*Blain et al.*, 2007] and Crozet [*Pollard et al.*, 2009] Island systems have corroborated the iron-dependency of elevated primary production and have indicated enhanced carbon flux from the surface ocean relative to adjacent HNLC control areas [*Blain et al.*, 2007; *Salter et al.*, 2007]. The enhanced sequestration of organic carbon beyond the ventilation depth to the deep ocean from a naturally fertilized bloom was observed for the first time during the Crozet experiment [*Pollard et al.*, 2009; *Salter*, 2008] confirming a measurable increase in the strength of the biological carbon pump in response to iron fertilization.

[5] In order to understand the mechanisms of enhanced carbon export to the deep-ocean in response to natural iron fertilization, it is necessary to identify the dominant phytoplankton involved. Diatoms are considered to be principal agents of the biological carbon pump in the Southern Ocean and are the key responders to both artificial and natural iron fertilization [*de Baar et al.*, 2005]. Yet there is debate about the relative efficiency of diatoms in exporting carbon as opposed to silica from the surface ocean through variation in diatom cellular Si/C ratios [*Ragueneau et al.*, 2006] that appear to be regionally and ecologically as well as physiologically controlled [*Baines et al.*, 2010] and specifically through the occurrence of empty frustules amongst surface populations (for example, in surface waters around Crozet, individual species represented as much as 50% by empty frustules; [*Poulton et al.*, 2007]. To inform models of the Southern Ocean carbon cycle it is important to characterize the key species that most efficiently operate the biological carbon pump, rather than simply those that dominate surface populations or those that primarily act as a vector for opal. Furthermore, diatom community structure around Southern Ocean island systems may differ markedly from open ocean Antarctic waters. Specifically, the centric diatom *Eucampia antarctica* that generally represents a small component of diatom flora in the open Southern Ocean [*Assmy et al.*, 2007; *Burckle*, 1984] exhibits enhanced abundance and may dominate blooms close to island systems including South Georgia [*Froneman et al.*, 1997; *Korb et al.*, 2008; *Ward et al.*, 2007], Crozet [*Poulton et al.*, 2007; *Salter et al.*, 2007] and Kerguelen [*Armand et al.*, 2008a; *Fryxell*, 1991].

[6] The objectives of this study were to use moored deep-ocean sediment traps to characterize the mechanisms and effectiveness of the marine biological carbon pump from the Fe-fertilized blooms around the Crozet Islands and in an adjacent HNLC control area to the south. Carbon and silica fluxes were quantified and the degree of coupling of the C and Si cycles assessed. Diatom export assemblages were analyzed to identify the role of key species in mediating carbon flux. The state of organic matter degradation was analyzed to determine the most effective pathway of carbon export to the deep ocean.

2. Study Area

[7] The Crozet Islands form part of a larger plateau that is located in 4200 m of water in the Southern Ocean at 46°S, 52°E. The archipelago is situated in the northern part of the Indian sector of the Southern Ocean (Figure 1a). The Crozet Islands and Plateau (hereafter Crozet), located in the Polar Frontal Zone (PFZ) at the northern boundary of the Southern Ocean, is a region characterized by a marked annual phytoplankton bloom (Figure 1b). Circulation patterns in the region are affected by local topography, the Antarctic Circumpolar Current (ACC), and zonal wind fields [*Pollard et al.*, 2007]. The sub-Antarctic Front (SAF), a major branch of the ACC, marks a locus of eastwards flow south of Del Cano Rise that is deflected northwards into the Crozet basin turning eastward again and combining with the Agulhas Return Current and the sub-Tropical Front, creating an S-bend feature (Figure 1b). South of this S-bend and north of the plateau itself mean circulation is weak with a residence time of ca. 60 days [*Pollard et al.*, 2007], allowing dissolved iron from the land or sediments of the Crozet Plateau to accumulate throughout the winter in the PFZ between Crozet and the SAF [*Planquette et al.*, 2007]. With excess macronutrients present in the HNLC waters this facilitates an annual bloom to north of the plateau; as evidenced from composite satellite imagery (Figure 1b).

[8] Deep-ocean sediment traps were deployed to the north of Crozet plateau beneath the iron replete [+Fe] bloom (M10 and M5) and in the iron deplete [−Fe] HNLC control area (M6) to the south (Figure 1b and Tables 1a–1c). The sediment traps were deployed at 2000, 3195, and 3160 m with bottom depths of 2935, 4277, and 4221 m at M10, M5 and M6, respectively. Throughout the remainder of the manuscript we use the following nomenclature to refer to the sediment trap deployment locations: M10[+FE]-N, M5 [+Fe]-NE and M6[−Fe]-S (Figure 1b).

3. Methods

3.1. Sediment Traps

[9] Deep-ocean sediment traps were deployed as part of the CROZEX (The Crozet Natural Iron Bloom and Export Experiment) and Benthic Crozet research programs. The traps were deployed in November 2004 on cruise D285 and recovered in January 2006 on cruise D300; both cruises were on the British research vessel R.R.S *Discovery*. The traps consist of plastic funnels with a baffle at the top (0.5 m^2 surface area) and a narrow opening at the bottom through which the particles fall into individual 250 mL sampling cups (McLane, Parflux 21 cup). Deployment schedules were programmed with a sampling resolution of 7 to 28 days (Tables 1a–1c) to reflect anticipated periods of high and low flux. The 250 mL sample cups were filled with a preservative solution, prepared by adding 100 g of analytical grade NaCl to 19 L of unfiltered deep (>2000 m) seawater from the trap deployment locations. One liter of formaldehyde (AnalR® grade, VWR international) was buffered to pH 8.6 with sodium tetraborate and added to the

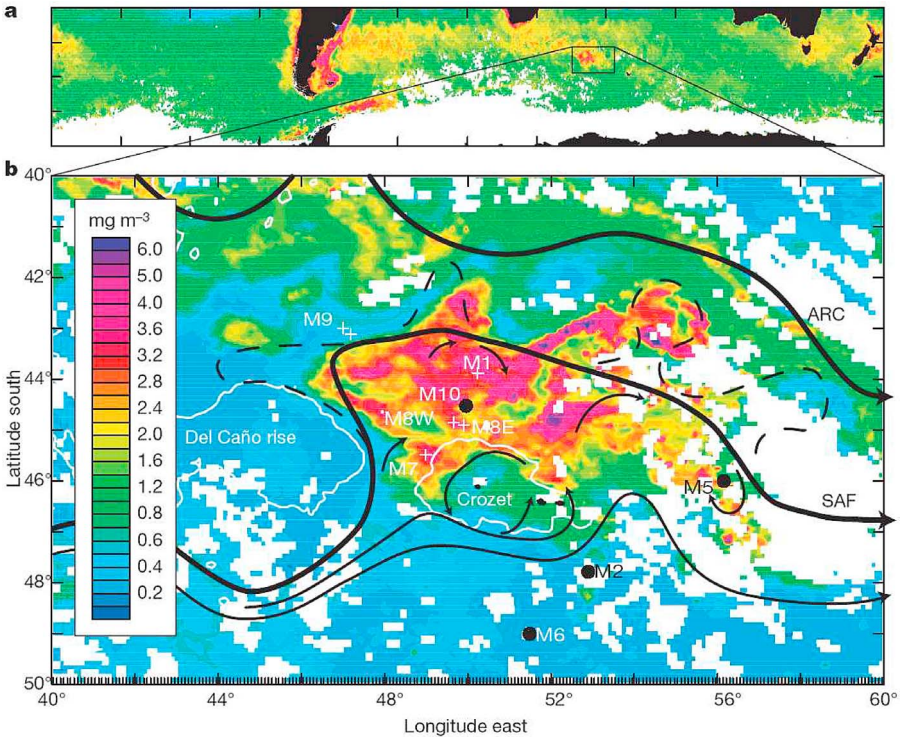

Figure 1. (a) Satellite composite of chlorophyll a for the month of October for the Southern Ocean, showing the location of Crozet. Color indicates Chl a concentration as shown in scale bar in Figure 1b. (b) Merged SeaWiFS/MODIS (sea-viewing, wide-field-of-view sensor/moderate-resolution imaging spectroradiometer) chlorophyll a image for the eight-day peak bloom period 23–30 October 2004. Solid and dashed lines show mean and eddy circulations, respectively, with the sub-Antarctic Front (SAF, the northern boundary of the Antarctic Circumpolar Current) and the Agulhas Return Current (ARC) shown bold. Sediment trap deployment locations are marked as M10 ([+FE]-N), M5 ([+Fe]-NE), M6 ([−FE]-S) and M2. Thin white lines are the 2,000-m depth contour, with the main Crozet Islands (Île de la Possession, Île de l'Est) seen at 46.5°S, 52°E. Coordinates for sediment trap deployment locations are: M10, 44° 29.95′ S, 49° 59.92′ E; M5, 46° 00.00′ S, 56° 05.00′ E; M6, 49° 00.03′ S, 51° 30.59′ E. Image modified from work by *Pollard et al.* [2009].

Table 1a. Sediment Trap Opening and Closing Times, Deployment Intervals, Total Mass, Particulate Organic Carbon (POC), Total Nitrogen (TN), Biogenic Silicon (BSi) and Degradation Index for Sediment Traps Deployed at M10[+Fe]-N-2000 m

M10[+Fe]-N Depth: 2000-m	Open Date (dd/mm/yyyy)	Close Date (dd/mm/yyyy)	Sampling Interval (days)	Total Mass Flux (mg m^{-2} d^{-1})	POC Flux (μmol m^{-2} d^{-1})	TN Flux (μmol m^{-2} d^{-1})	BSi Flux (mmol m^{-2} d^{-1})	DI
M10-A-1	21/12/2004	02/01/2005	12	225	472	60	2.6	n.d.[a]
M10-A-2	02/01/2005	16/01/2005	14	155	333	38	1.4	n.d.
M10-A-3	16/01/2005	30/01/2005	14	147	319	29	1.1	n.d.
M10-A-4	30/01/2005	20/02/2005	21	76	339	48	0.46	n.d.
M10-A-5	20/02/2005	20/03/2005	28	41	229	38	0.24	n.d.
M10-A-6	20/03/2005	17/04/2005	28	23	111	19	0.13	n.d.
M10-A-7	17/04/2005	15/05/2005	28	n.d.	n.d.	n.d.	n.d.	n.d.
M10-A-8	15/05/2005	12/06/2005	28	n.d.	n.d.	n.d.	n.d.	n.d.
M10-A-9	12/06/2005	10/07/2005	28	n.d.	n.d.	n.d.	n.d.	n.d.
M10-A-10	10/07/2005	07/08/2005	28	n.d.	n.d.	n.d.	n.d.	n.d.
M10-A-11	07/08/2005	04/09/2005	28	n.d.	n.d.	n.d.	n.d.	n.d.
M10-A-12	04/09/2005	02/10/2005	28	n.d.	n.d.	n.d.	n.d.	n.d.
M10-A-13	02/10/2005	16/10/2005	14	n.d.	n.d.	n.d.	n.d.	n.d.
M10-A-14	16/10/2005	30/10/2005	14	n.d.	n.d.	n.d.	n.d.	n.d.
M10-A-15	30/10/2005	13/11/2005	14	n.d.	n.d.	n.d.	n.d.	n.d.
M10-A-16	13/11/2005	27/11/2005	14	n.d.	n.d.	n.d.	n.d.	n.d.
M10-A-17	27/11/2005	08/12/2005	11	119	469	78	0.90	n.d.

[a]Not determined.

Table 1b. Sediment Trap Opening and Closing Times, Deployment Intervals, Total Mass, Particulate Organic Carbon (POC), Total Nitrogen (TN), Biogenic Silicon (BSi) and Degradation Index for Sediment Traps Deployed at M5[+Fe]-NE-3195 m

M5[+Fe]-NE Depth: 3195-m	Open Date (dd/mm/yyyy)	Close Date (dd/mm/yyyy)	Sampling Interval (days)	Total Mass Flux (mg m^{-2} d^{-1})	POC Flux (μmol m^{-2} d^{-1})	TN Flux (μmol m^{-2} d^{-1})	BSi Flux (mmol m^{-2} d^{-1})	DI
M5-B-1	28/12/2004	09/01/2005	12	131	244	41	1.3	0.5
M5-B-2	09/01/2005	23/01/2005	14	143	223	32	1.5	0.4
M5-B-3	23/01/2005	06/02/2005	14	237	330	61	2.6	0.4
M5-B-4	06/02/2005	27/02/2005	21	146	186	33	1.4	0.3
M5-B-5	27/02/2005	27/03/2005	28	148	211	49	1.3	0.4
M5-B-6	27/03/2005	24/04/2005	28	11	19.0	3.4	0.08	n.d.
M5-B-7	24/04/2005	22/05/2005	28	59	127	17	0.39	n.d.
M5-B-8	22/05/2005	19/06/2005	28	23	247	31	0.11	0.9
M5-B-9	19/06/2005	17/07/2005	28	1.1	12.9	1.8	n.d.	n.d.
M5-B-10	17/07/2005	14/08/2005	28	0.81	15.6	1.7	n.d.	n.d.
M5-B-11	14/08/2005	04/09/2005	21	0.94	16.0	1.4	n.d.	n.d.
M5-B-12	04/09/2005	25/09/2005	21	n.d.	n.d.	n.d.	n.d.	n.d.
M5-B-13	25/09/2005	16/10/2005	21	1.3	19.8	1.4	n.d.	n.d.
M5-B-14	16/10/2005	30/10/2005	14	0.51	1.46	0.23	n.d.	n.d.
M5-B-15	30/10/2005	13/11/2005	14	0.96	4.83	0.76	n.d.	n.d.
M5-B-16	13/11/2005	27/11/2005	14	n.d.	n.d.	n.d.	n.d.	n.d.
M5-B-17	27/11/2005	11/12/2005	14	0.43	0.52	0.30	n.d.	n.d.
M5-B-18	11/12/2005	18/12/2005	7	0.86	2.09	0.32	n.d.	n.d.
M5-B-19	18/12/2005	20/12/2005	2	793	3946	642	4.6	−0.7
M5-B-19*[a]	18/12/2005	29/12/2005[a]	11[a]	99[a]	493[a]	80[a]	0.58[a]	−0.7

[a]See Figure 2 caption for explanation of 38-B-19.

19 L of hyper-saline seawater, and the solution left to stand for a period of 1 day [*Salter*, 2008].

[10] Upon recovery samples were filtered through a 1 mm Nitex mesh. Swimmers were carefully removed from the <1 mm fraction. The >1 mm size fraction was comprised exclusively of large swimmers. Some cups were contaminated by fish (*Notolepis coatsi*) feeding on the sinking material. All fish debris was picked out by hand. Previous analysis rejected data from M2 [*Pollard et al.*, 2009; *Salter*, 2008] (Figure 1) due to serious contamination by fish debris. Although certain qualitative analyses related to the determination of annual export estimates utilize data from M2 no further discussion of this data will take place.

[11] All chemical analysis was performed on the <1 mm fraction. The 250 mL samples were split into eight aliquots of equal volume using a McLane rotary splitter. According to sample mass, one to five of these eighths were filtered onto cellulose nitrate filters (47 mm, 0.45 μm pore size) and the filtrate from one aliquot stored in a clean LDPE bottle (60 mL). The samples and filters were subsequently rinsed with a 0.56 M ammonium formate solution (pH 7) to remove excess sea-salt and formalin. The sample was carefully

Table 1c. Sediment Trap Opening and Closing Times, Deployment Intervals, Total Mass, Particulate Organic Carbon (POC), Total Nitrogen (TN), Biogenic Silicon (BSi) and Degradation Index for Sediment Traps Deployed at M6[−Fe]-S-3160 m

M6[−Fe]-S Depth: 3160-m	Open Date (dd/mm/yyyy)	Close Date (dd/mm/yyyy)	Sampling Interval (days)	Total Mass Flux (mg m^{-2} d^{-1})	POC Flux (μmol m^{-2} d^{-1})	TN Flux (μmol m^{-2} d^{-1})	BSi Flux (mmol m^{-2} d^{-1})	DI
M6-B-1	05/01/2005	16/01/2005	11	505	640	96	6.7	0.5
M6-B-2	16/01/2005	30/01/2005	14	0.67	2.2	0.28	n.d.	n.d.
M6-B-3	30/01/2005	13/02/2005	14	0.27	0.13	0.05	n.d.	n.d.
M6-B-4	13/02/2005	06/03/2005	21	3.9	7.6	1.1	n.d.	n.d.
M6-B-5	06/03/2005	03/04/2005	28	0.44	1.0	0.17	n.d.	n.d.
M6-B-6	03/04/2005	01/05/2005	28	40	207	30	0.50	n.d.
M6-B-7	01/05/2005	29/05/2005	28	0.89	15	1.4	n.d.	n.d.
M6-B-8	29/05/2005	26/06/2005	28	0.31	5.0	0.57	n.d.	n.d.
M6-B-9	26/06/2005	24/07/2005	28	0.22	2.2	0.34	n.d.	n.d.
M6-B-10	24/07/2005	21/08/2005	28	0.24	1.2	0.19	n.d.	n.d.
M6-B-11	21/08/2005	11/09/2005	21	0.29	8.7	0.79	n.d.	n.d.
M6-B-12	11/09/2005	02/10/2005	21	0.47	1.2	0.28	n.d.	n.d.
M6-B-13	02/10/2005	16/10/2005	14	0.59	1.4	0.23	n.d.	n.d.
M6-B-14	16/10/2005	30/10/2005	14	0.53	0.74	0.08	n.d.	n.d.
M6-B-15	30/10/2005	13/11/2005	14	0.21	0.19	0.07	n.d.	n.d.
M6-B-16	13/11/2005	27/11/2005	14	0.50	1.5	0.41	n.d.	n.d.
M6-B-17	27/11/2005	11/12/2005	14	0.43	0.77	0.18	n.d.	n.d.
M6-B-18	11/12/2005	18/12/2005	7	1.4	11	2.5	n.d.	n.d.
M6-B-19	18/12/2005	25/12/2005	7	0.91	1.1	0.42	n.d.	n.d.
M6-B-20	25/12/2005	01/01/2006	7	0.74	1.9	0.42	n.d.	n.d.
M6-B-21	01/01/2006	03/01/2006	2	3.4	20	2.6	n.d.	n.d.

removed with a metal spatula as a wet cake of material and transferred to pre-combusted (450°C; 12 hours) glass vials and frozen at −20°C. Frozen samples were freeze-dried over night and homogenized to a fine powder. This material was used to weigh samples for the determination of particulate organic carbon (POC), total carbon (TC), biogenic silicon (BSi), and total hydrolysable amino acids (THAA). Total mass flux was determined gravimetrically following the filtration of a 1/8th aliquot onto a pre-weighed cellulose nitrate filter (47 mm diameter, 0.45 μm pore size). The filter was rinsed with 0.56 M ammonium formate (pH 7) to remove salt and excess formalin and dried at 60°C until a constant weight was achieved.

3.2. Particulate Organic Carbon (POC)

[12] POC was determined using a Carlo-Erba NA-1500 elemental analyzer following standardization with acetanilide. Freeze-dried samples (2–4 mg) were weighed into pre-combusted (12 hours at 450°C) silver cups which were formed into small capsules with metal spatulas. Organic carbon was determined on acidified samples [*Nieuwenhuize et al.*, 1994] where 15 μL aliquots of 20% HCl were added to the sample in order to remove calcium carbonate. After each aliquot was added the acid was evaporated by gently heating on a hot plate (<60°C). The procedure was repeated until all carbonates were removed as evidenced by the absence of any effervescence upon addition of the acid, and then two more additions of acid were performed to ensure complete removal of inorganic carbon. Samples were subsequently rinsed with 5 × 40 μL aliquots of ultra-pure water and dried on a hotplate at <60°C, and then at 50°C overnight. Care was taken to note any sample loss from silver cups and samples discarded if this was the case [*Salter*, 2008]. Selected samples were analyzed independently at the University of Liverpool, UK (UOL). Excellent data correlations were observed for both total carbon ($r = 0.96$, $p < 0.001$, $n = 15$) and organic carbon ($r = 0.97$, $p < 0.001$, $n = 15$). The average analytical precision (relative error) from 106 sets of triplicate measurements (including samples from the NE Atlantic [*Salter et al.*, 2010]) was 4.3% for organic carbon and 2.1% for total carbon analyses.

3.3. Biogenic Silicon (BSi)

[13] Silicon of biogenic origin (BSi) was determined using a wet chemical technique modified from [*Mortlock and Froelich*, 1989]. Samples (3–5 mg) were weighed into clean polypropylene tubes. Particulate opal ($SiO_2.nH_20$) was converted into dissolved metasilicate (SiO_3^{-2}) using a 0.2 mol L^{-1} sodium hydroxide extraction for 3 hours at 100°C. The extract solution was separated from the residue via centrifugation and the sediment residue was rinsed with ultra pure water and dried overnight (60°C). The dissolved silicate was converted to the silico-molybdate complex [*Strickland and Parsons*, 1968] and the absorbance read at 812 nm with a Hitachi U-2000 spectrophotometer.

[14] The extraction method described here was tested on reference material from an inter-laboratory comparison experiment [*Conley*, 1998]. A paired Student's *t*-test showed there was no significant difference between the average values originating from the inter-laboratory comparison and those obtained with this extraction method [*Salter*, 2008]. At low biogenic silica ($BSiO_2$) concentrations (<10%), Si leached from aluminosilicates may slightly overestimate $BSiO_2$ content [*Fabres et al.*, 2002]. This problem has a minor effect on the analysis presented here since all samples had $BSiO_2$ contents > 10% with correspondingly low aluminosilicate contents.

[15] In order to check the effect of Si-leaching from aluminosilicates on biogenic silicon content, and as a second check on the extraction efficiency of this method, sediment cores from the Southern Ocean were analyzed. Values obtained with the method were compared with those deduced from a three-component mixing model, in which $BSiO_2$ concentrations were calculated by difference from measured $CaCO_3$ and lithogenic components. Excellent agreement ($r = 0.86$, $n = 19$, $p < 0.001$) was observed between the two methods for all the samples analyzed (including samples from the NE Atlantic [*Salter et al.*, 2010], which covered the range of 10–90% SiO_2 [*Salter*, 2008]). The average analytical precision (relative error) from 101 sets of triplicate measurements was 4.2% for BSi analyses.

3.4. Total Hydrolysable Amino Acids and Hexosamines

[16] Particulate amino acids were hydrolyzed from freeze-dried material following the method of [*Cowie and Hedges*, 1992]. Hydrochloric acid (3 mL; 6 mol L^{-1}) was added to 5–15 mg of freeze-dried sediment trap material in 7 mL glass vials (Supelco) [*Cowie and Hedges*, 1992; *Gupta and Kawahata*, 2000]. Before addition to the sediment the hydrochloric acid was degassed by gently bubbling pure argon through the solution for thirty minutes. The headspace in the vials was displaced by argon and the glass vials sealed and heated at 110°C for 24 hours. The vials were removed from the heat source and allowed to cool for ten minutes. After centrifugation at 3000 revolutions per minute (rpm) for 15 min, 1 mL of the hydrolyzate was transferred to a microcentrifuge tube (1.5 mL Eppendorf) and stored at −80°C for analysis. On the day of analysis 250 μL of hydrolyzate was neutralized with 1 mol L^{-1} NaOH, and diluted with ultra pure water and syringe-filtered (0.2 μm; Fisher Scientific). 280 μL of the neutralized sample or standard was added to a HPLC vial (Sigma Aldrich), followed by 15 μL of 1.25 μmol L^{-1} *o*-methyl-threonine as an internal standard and 15 μL of 0.04 mol L^{-1} boric acid buffer (pH 8.3).

[17] Amino acids were analyzed by High Performance Liquid Chromatography (HPLC, Shimadzu) using pre-column (*o*- Phthaldialdehyde [OPA]) derivatization after acid hydrolysis [*Cowie and Hedges*, 1992; *Lindroth and Mopper*, 1979]. Amino acids were separated on an Ascentis C_{18}, 15 cm × 4.6 mm × 3 μm reverse-phase column with a mobile phase flow rate of 1 mL min^{-1}. The analytical column was maintained at a constant temperature of 30°C and fitted with an Alltech guard column. A binary gradient of methanol (eluant A) and 30 mmol L^{-1} Na-acetate (pH 7) and 2% tetrahydrofuran (THF) (eluant B) was used to achieve chromatographic resolution. Amino acids were identified and quantified by comparison to analytical standards (Sigma-Aldrich). All sample and standard peak areas were normalized to the response of the internal standard *o*-methyl-threonine. After normalization standard calibrations for all individual amino acids had a regression coefficient >0.98. The amino acid OPA derivatives were

formed online and detected by fluorescence using an excitation wavelength of 360 nm and monitoring emission wavelengths at 430 nm [*Cowie and Hedges*, 1992; *Salter*, 2008; *Salter et al.*, 2010].

[18] For most amino acids, detected operational blank values were <2% of sample concentrations. For methionine, valine, and ornithine blank concentrations represented 5.7%, 8.5%, and 49.8% of sample concentrations. The high blank value for ornithine has a negligible effect on the results because it is a small component of the total amino acid pool. Long-term statistical reproducibility calculated from repeat hydrolyzation and analysis of the same sample was better than 10% for total hydrolysable amino acids. The average analytical precision (relative error) from 83 sets of duplicate measurements was 12.3% for total hydrolysable amino acids.

3.5. Principal Components Analysis

[19] Principal components analysis (PCA) is a multivariate statistical method designed to reduce a large number of variables to a few principle components. The first principle component describes the maximum amount of variability within a data-set with successive components describing progressively less variability. Following [*Dauwe et al.*, 1999] PCA was used to investigate the variation in amino acid composition among sediment trap samples that were collected at different times. The variables (mol % of individual THAAs) were standardized prior to performing PCA [*Dauwe et al.*, 1999; *Ingalls et al.*, 2006] by subtracting the mean of all values and dividing by the standard deviation of all values [*Sheridan et al.*, 2002]. The Degradation Index (DI) is calculated according to equation (1) [*Dauwe et al.*, 1999]:

$$\mathrm{DI} = \sum \left[\left(\frac{\mathrm{Var_i} - \mathrm{AvgVar_i}}{\mathrm{StdVar_i}} \right) \times \mathrm{Loading_i} \right] \quad (1)$$

where, $\mathrm{Var_i}$ is the mol % of amino acid i, $\mathrm{AvgVar_i}$ and $\mathrm{StdVar_i}$ are the mean and standard deviation of amino acid i (mol%) and $\mathrm{Loading_i}$ is the PCA-derived loading of amino acid *i* [*Salter et al.*, 2010]. The summation includes all amino acids examined. The PCA-derived loading in equation (1) is a measure of a variables contribution to the variability of the data-set. [*Dauwe et al.*, 1999] derived these loadings from the PCA of a data set that contained samples of varying degrees of degradation including plankton, particulate matter and sediments.

3.6. Diatom Flux Assemblages, Microscopy and Taxonomy

[20] A 1/8th aliquot of each sediment trap sample was designated for phytoplankton taxonomy. The volume of the aliquot was recorded prior to removal of any material. The aliquot was shaken thoroughly to re-suspend the particulate slurry and 1–2 mL were removed with a modified pipette tip and transferred to a 60 mL LDPE bottle containing 19 mL of 0.2 μm filtered preservative solution. The pipette tip was rinsed with a known volume of clean preservative solution to remove any material adhering to the interior surfaces. The standard pipette tip (5 mL) had the bottom 1 cm removed to increase the diameter of the tip aperture and thus minimize selective removal of certain particle sizes. The 10 mL sub-samples were settled in chambers (Hydro-Bios) for ~10–12 hrs and examined using a Brunel Microscopes SP-95-I inverted microscope. Large and numerically rare taxa were counted during full examination of the settling chamber at high magnification (×100), while smaller (<50 μm) and numerically dominant taxa were counted on 1–2 transects of the chamber (×100, ×200) or from cumulative counts from several (5–10) fields of view (×400). Diatoms were identified to genera or species following [*Poulton et al.*, 2007; *Priddle and Fryxell*, 1985; *Tomas*, 1997]. For very large diatoms, whole cells and half cells were counted for *Corethron* sp and whole cells only for *Dactyliosolen* sp. The centric diatoms *Thalassiosira* spp. and *Coscinodiscus* spp. were not differentiated and were counted as centrics > or < 50 microns (Table 3). *Eucampia antarctica* was present as the sub-polar variety *E. antarctica* var. *antarctica* [*Fryxell and Prasad*, 1990], characterized primarily by asymmetry of the valves in girdle view (Figure 4). The *E. antarctica var. ant.* valves comprised almost exclusively the heavily silicified resting spores (or winter growth stages) with only rare occurrences of the vegetative stages.

[21] Individual diatom fluxes were calculated according to equations (2) and (3)

$$\mathrm{TSp_i} = \mathrm{CSp_i} \times \left[\frac{(\mathrm{D_{Vol}} + \mathrm{C_{Vol}})}{\mathrm{C_{Vol}}} \right] \times 8 \quad (2)$$

where $\mathrm{TSp_i}$ is the total number of species i valves in the 250 mL sediment trap sampling cup, $\mathrm{CSp_i}$ is the number of species i valves enumerated in the 10 mL settling chamber (valves $\mathrm{mL^{-1}}$), $\mathrm{D_{Vol}}$ is the sum of the volume of filtered preservative solution used as a dilution and rinsing medium (mL), $\mathrm{C_{Vol}}$ is the volume of sediment trap aliqout slurry taken for dilution (mL) and 8 is a constant factor to correct for the 1/8th split methodology.

$$\mathrm{FSp}i = [\mathrm{TSp}i/\mathrm{A}]/\mathrm{t} \quad (3)$$

Where $\mathrm{FSp_i}$ is the flux of species i in valves $\mathrm{m^{-2}\ d^{-1}}$, A is the area of the sediment trap collecting aperture in $\mathrm{m^2}$, and t is the sampling interval in days.

3.7. Calculation of Annual Export Fluxes

[22] To estimate annual export fluxes for the various biogenic components it was necessary to assess any period of "unsampled" flux caused by the logistical constraints of sediment trap deployment and recovery schedules. To do this we determined (1) the probable date for the onset of flux from the surface ocean and (2) the probable settling velocities of particles.

[23] (1) Peaks in satellite-derived chlorophyll *a* data provide a good approximation for the start of phytoplankton biomass decline in the surface ocean, particularly at the Crozet site since there was a strong correlation between satellite-derived chlorophyll and euphotic-zone integrated primary production [*Seeyave et al.*, 2007]. In Figures 2a, 2c, and 2e the timing of chl *a* peaks are identified by the black and white arrows for 2004 and 2005, respectively. The calculations which follow have assumed these peaks in chl *a* to

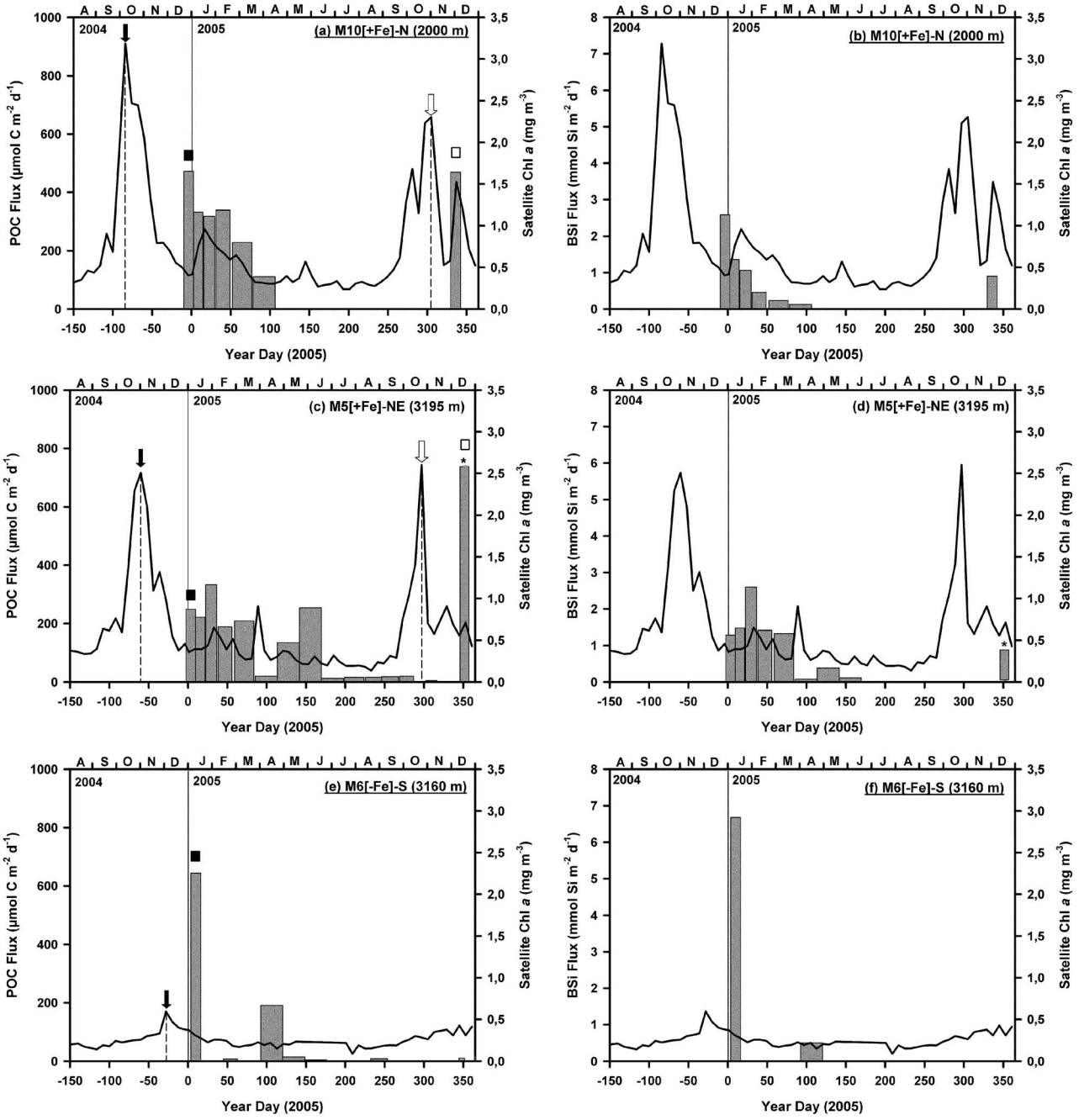

Figure 2. Gray bars are export of particulate organic carbon (Figures 2a, 2c, and 2e) and Si (Figures 2b, 2d, and 2f) to the deep-ocean at (a and b) M10[+FE]-N (2000 m), (c and d) M5[+Fe]-NE (3195 m), and (e and f) M6[−Fe]-S (3160 m). Black lines are satellite-derived chl a, calibrated with in-situ measurements [*Venables et al.*, 2007] at each sediment trap deployment location. Black and white arrows mark the peaks of Chl a in 2004 and 2005, respectively. Black and white squares mark the beginning of export flux in 2004 and 2005, respectively (see equations (4)–(8)). The data point marked with an asterisk in Figures 2c and 2d is 38-B19 and has been adjusted for sample interval time by comparison with M10[+Fe]-N data (Table 1b).

indicate the probable starting point of export flux from the surface ocean.

[24] (2) Particle settling velocities were approximated by calculating signal propagation velocities [*Armstrong et al.*, 2009] from particle flux and satellite chl *a* data specific to each sediment trap deployment location (Figure 2). At M10 [+Fe]-N and M5[+Fe]-NE the first export flux signal in 2005 is marked by a white square in Figures 2a and 2c. Note that any export flux prior to these dates was negligible (Tables 1a–1c) and we can therefore be certain that these

signals represent the initial export fluxes from the 2005 bloom (Figures 2a and 2c). Signal propagation velocities at the [+Fe] sites were calculated in the following ways: (1) comparing the 2005 chl *a* peak with the 2005 export flux signal at M10[+Fe]-N (equation (4)), (2) comparing the 2005 chl *a* peak with the 2005 export flux signal at M5[+Fe]-NE (equation (4)), or (3) comparing the first export flux signals in 2005 from the M10[+Fe]-N (2000 m) and M5[+Fe]-NE (3195 m) traps (equation (5)). At M6[−Fe]-S, due to the absence of a flux signal at the end of 2005 (Figure 2e), chl a and export signals from 2004 were used. Export flux data from M2 (2000 m) (Figure 1b) were used for M6[−Fe]-S in equation (5). The simple presence of an export flux event at M2 (2000 m) was deemed reliable enough to calculate a signal propagation velocity, however further analysis of M2 was rejected due to serious sample contamination by fish [*Pollard et al.*, 2009; *Salter*, 2008].

$$\mathrm{Ws} = \frac{[(^{\mathrm{ST}}\mathrm{F}_{\mathrm{START}}) - (^{\mathrm{ST}}\mathrm{P}_{\mathrm{CHL}})]}{^{\mathrm{ST}}\mathrm{D}_{\mathrm{TRAP}}} \tag{4}$$

$$\mathrm{Ws} = \frac{\left[\left(^{[+\mathrm{Fe}]-\mathrm{NE}}\mathrm{F}_{\mathrm{START}}\right) - \left(^{[+\mathrm{Fe}]-\mathrm{N}}\mathrm{F}_{\mathrm{START}}\right)\right]}{\left[\left(^{[+\mathrm{Fe}]-\mathrm{NE}}\mathrm{D}_{\mathrm{TRAP}}\right) - \left(^{[+\mathrm{Fe}]-\mathrm{N}}\mathrm{D}_{\mathrm{TRAP}}\right)\right]} \tag{5}$$

where Ws is particle settling velocity (m d^{-1}), F_{START} is the timing of the first export flux signal (year day), P_{CHL} is the timing of the peak in chl *a* (year day), D_{TRAP} is the deployment depth (m) of the sediment trap (Tables 1a–1c), and ST denotes either M10[+Fe]-N, M5[+Fe]-NE, or M6[−Fe]-S sediment traps.

[25] The number of days of "unsampled" flux in 2004 were computed as a function of the calculated Ws values (Table 2) according to equation (6):

$$\mathrm{M} = \left(^{\mathrm{ST}}\mathrm{F}_{\mathrm{START}}\right) - \left[\left(\frac{^{\mathrm{ST}}\mathrm{D}_{\mathrm{TRAP}}}{\mathrm{Ws}}\right) + \left(^{\mathrm{ST}}\mathrm{P}_{\mathrm{CHL}}\right)\right] \tag{6}$$

where M is the "unsampled" flux period (days), $^{ST}F_{START}$ is the year day in 2004 at the beginning of the trap deployment when export flux was first recorded (black square in Figures 2a, 2c, and 2e), $^{ST}D_{TRAP}$ is the deployment depth of the sediment trap (m), Ws is the estimated settling velocity (m d^{-1}) (equations (4) and (5)), P_{CHL} is the year day of peak chl *a* occurrence in 2004 (black arrows in Figures 2a, 2c, and 2e) and ST represents either of the sediment trap sites M10[+Fe]-N, M5[+Fe]-NE or M6[−Fe]-S.

[26] Following the estimation of the "unsampled" flux period (equation (6)), export fluxes were extrapolated using biogeochemical data according to equations (7) and (8).

$$[\mathrm{M} + \mathrm{F_I}] \times \mathrm{E}(i) \tag{7}$$

where M is the "unsampled" flux period (days), F_I is the export flux sampling interval (days) of the extrapolated flux measurement, and E is the measured export flux of either POC, Si, or TN *(i)* (mol m^{-2} d^{-1}). The specific flux measurements that were extrapolated to compute annual fluxes are M10-A-17 [+Fe]-N, M5-B-19* [+Fe-NE] (see Figure 2 caption), and M6-B-1 [−Fe]-S (Tables 1a–1c). Annual fluxes were subsequently calculated according to equation (8):

$$\text{Annual flux } (i) = \sum [\mathrm{F_I} \times \mathrm{E}(i)] \tag{8}$$

4. Results

4.1. POC Export Flux

[27] The magnitude and seasonality of deep-water POC export flux in the [+Fe] and [−Fe] regions of the Crozet Plateau exhibited strong differences (Figures 2a, 2c, and 2e and Tables 1a–1c). At M6[−Fe]-S POC export was characterized by discrete flux events, of which the major event occurred in January (year day 5 to 16) contributing 50% of the annual POC flux (Table 1c). The POC export flux during this period was 640 μmol C m^{-2} d^{-1}. A second discrete POC flux event of 207 μmol C m^{-2} d^{-1} accounted for 41% of the annual flux. Aside from these two dominant features, POC fluxes for the remainder of the year, which covered a period of 322 days, were negligible accounting for <10% of annual POC export flux (Figure 2e and Table 1c).

[28] POC export fluxes at M10[+Fe]-N and M5[+Fe]-NE were generally smaller and less espisodic than those observed at M6[−Fe]-S but were sustained over a longer period of time (Figures 2a and 2c). At M10[+Fe]-N a maximum flux of 472 μmol C m^{-2} d^{-1} was observed at the end of December 2004 (year day −9 to 3), thereafter POC fluxes gradually declined over a period of 100 days until mid-April 2005 (year day 107) (Figure 2a and Table 1a). A similar pattern of flux was observed at M5[+Fe]-NE (Figure 2c and Table 1b), although here the export fluxes continued to decline for a period of 150 days until mid-June (year day 170).

4.2. BSi Export Flux

[29] At M10[+Fe]-N and M5[+Fe]-NE BSi fluxes ranged between 0.13–2.6 and 0.11–2.6 mmol Si m^{-2} d^{-1} respectively, compared to 0.50–6.7 mmol Si m^{-2} d^{-1} at M6[−Fe]-S (Figures 2b, 2d, and 2f and Tables 1a–1c). Similar to POC, BSi fluxes at M6[−Fe]-S were characterized by discrete events of large magnitude (Figure 2f and Table 1c). During the major export flux event which occurred in January at M6[−Fe]-S a BSi flux of 6.7 mmol Si m^{-2} d^{-1} was the highest observed during the study. The BSi fluxes at the [+Fe] sites were generally lower than those at the [−Fe] site but were sustained over a longer period of time (Figures 2b, 2d, and 2f).

4.3. Annual Export Fluxes, Si/C and Si/N Ratios

[30] Three different methods were used to estimate annual fluxes (section 3.7) and here we report the ranges resulting from those methods (Figure 3 and Table 2). Annual POC fluxes were comparable between the two [+Fe] sites and range from 37–60 and 40–42 mmol C m^{-2} yr^{-1} at M10[+Fe]-N and M5[+Fe]-NE, respectively, notably higher than the 14–21 mmol C m^{-2} yr^{-1} calculated at M6[−Fe]-S (Figure 3a). Patterns for total nitrogen fluxes were similar to POC (Table 2). The range of annual BSi fluxes were similar between the two [+Fe] and one [−Fe] sites (Figure 3b and

Table 2. Annually-Integrated Export Fluxes, Si/C and Si/N Ratios[a]

	Estimated Ws ($m\ d^{-1}$)	Extrapolation (days)	POC Flux ($mmol\ m^{-2}\ y^{-1}$)	TN Flux ($mmol\ m^{-2}\ y^{-1}$)	Si Flux ($mmol\ m^{-2}\ y^{-1}$)	Si/C (mol/mol)	Si/N (mol/mol)
			M10[+Fe]-N				
Normal	-	-	37	5.1	95	2.6	18
Trap/Trap signal	47	32	52	7.6	123	2.4	16
Chl/Trap signal	78	49	60	9.0	139	2.3	15
			M5[+Fe]-NE				
Normal	-	-	40	6.6	165	4.1	25
Trap/Trap signal	47	0	40	6.6	165	4.1	25
Chl/Trap signal	55	3	42	6.9	167	4.0	24
			M6[−Fe]-S				
Normal	-	-	14	2.1	87	6.4	42
Trap/Trap signal	125	9	20	2.9	148	7.6	50
Chl/Trap signal	140	12	21	3.2	168	7.8	52

[a]"Normal" is data obtained from integrating the data over the sediment trap deployment periods. Estimates for the period of missing flux are provided based on the timing of chlorophyll and export signals and signal propagation velocities (Ws) (equations (4)–(8)). Annual export fluxes and ratios are provided for extrapolations based on the propagation of chlorophyll and export signals (Chl/Trap) or from the comparison of export signals from different depths (Trap/Trap).

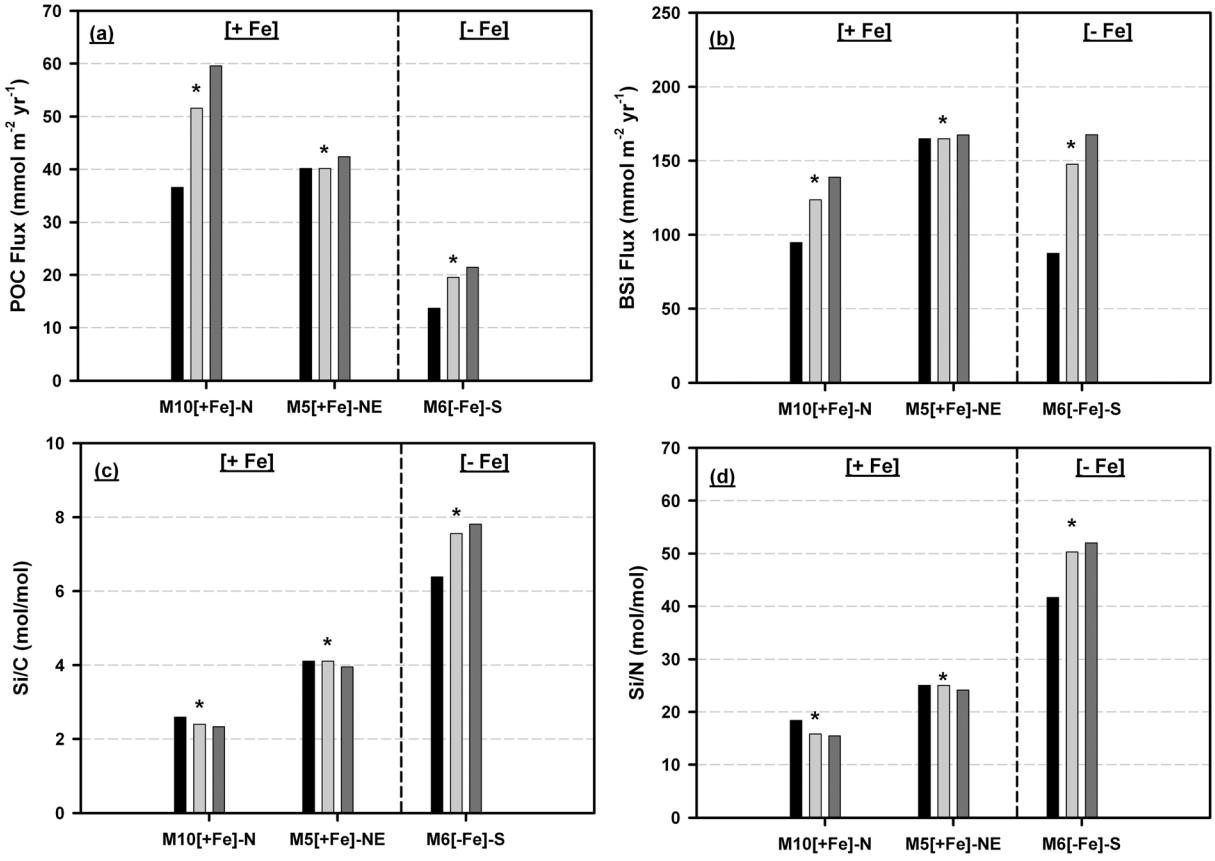

Figure 3. Annually-integrated fluxes of (a) particulate organic carbon (b) biogenic silicon (c) Si/C and (d) Si/N ratios at stations M10[+Fe]-N, M5[+Fe]-NE, and M6[−Fe]-S. Black bars are the annual fluxes and ratios obtained from integrating the data over the sediment trap deployment periods of 352, 361 and 361 days at M10[+Fe]-N, M5[+Fe]-NE, and M6[−Fe]-S, respectively. Gray bars are annual fluxes including an estimate for the period of missing flux based on the timing of chlorophyll and export signals and signal propagation velocities (equations (4)–(8)). Light gray bars are signal propagation velocities from comparison of export signals at different depths (equation (5)) and dark gray bars are signal propagation velocities from comparison of chlorophyll and export signals (equation (4)). See section 3.7 for further details.

Table 3. Fluxes (10^4 Valves m^{-2} d^{-1}) and Percentage Contribution of Diatom Export Assemblages

		Centric < 50 μm		Centric > 50 μm		*Chaetoceros* spp.[a]		*C. Pennatum*		*D. antarcticus*[b]	
Sample Code	Year Day (Mid-point)	Flux	Percent	Flux	Percent	Flux	Percent	Flux	Percent	Flux	Percent
					M10[+Fe]-N						
M10-A-1	362	2.3	0.1	0.8	<0.1	-[c]	-	28	1.1	-	-
M10-A-2	9	26	1.5	0.7	<0.1	-	-	13	0.7	0.7	<0.1
M10-A-3	23	14	0.8	8.3	0.5	-	-	3.8	0.2	-	-
M10-A-4	40	8.5	1.0	2.5	0.3	-	-	5.0	0.6	-	-
M10-A-5	65	3.6	1.0	1.4	0.4	-	-	0.4	0.1	-	-
M10-A-6	93	3.3	1.2	1.1	0.4	-	-	-	-	-	-
M10-A-17	336	29	2.9	-	-	-	-	0.5	0.1	-	-
					M5[+Fe]-NE						
M5-B-1	4	43	2.6	2.1	0.1	-	-	2.1	0.1	-	-
M5-B-2	16	38	2.3	1.2	0.1	-	-	9.5	0.6	-	-
M5-B-3	30	124	6.4	6.0	0.3	-	-	18	0.9	0.9	<0.1
M5-B-4	47	90	6.3	5.6	0.4	-	-	11	0.8	2.8	0.2
M5-B-5	72	61	5.5	7.5	0.7	-	-	8.1	0.7	1.9	0.2
M5-B-6	100	16	3.9	4.4	1.1	-	-	-	-	-	-
M5-B-7	128	24	3.3	4.5	0.6	-	-	0.8	0.1	0.3	<0.1
M5-B-8	156	7.2	2.3	1.9	0.6	-	-	-	-	-	-
M5-B-19*	353	106	3.7	8.3	0.3	-	-	0.9	0.03	0.9	<0.1
					M6[−Fe]-S						
M6-B-1	10	783	14	51	0.9	10	0.2	176	3.2	47	0.9
M6-B-6	107	36	4.7	4.3	0.6	-	-	6.0	0.8	2.6	0.3
Annual Fluxes	No. of Days	Flux	Percent	Flux	Percent	Flux	Percent	Flux	Percent	Flux	Percent
M10[+Fe]-N	352	1277	1.0	258	0.2	-	-	689	0.6	9.1	<0.1
M5[+Fe]-NE	361	8869	4.4	845	0.4	-	-	896	0.4	141	0.1
M6[−Fe]-S	361	9626	12	687	0.8	113	0.1	2105	2.5	593	0.7

	E. ant. var. *ant.*[d]		*F. kerguelensis*		*Membraneis* spp.		*Rhizosolenia* spp.		*Thalassiothrix* spp.		
Sample Code	Flux	Percent	Flux	Percent	Flux	Percent	Flux	Percent	Flux	Percent	Total Diatom Flux
					M10[+Fe]-N						
M10-A-1	1755	71	684	28	-[e]	-	0.8	<0.1	-	-	2471
M10-A-2	1032	61	625	37	0.7	<0.1	0.7	<0.1	-	-	1699
M10-A-3	1078	62	647	37	-	-	0.7	<0.1	-	-	1751
M10-A-4	537	60	335	38	-	-	0.5	0.1	-	-	888
M10-A-5	223	62	132	37	-	-	-	-	-	-	360
M10-A-6	111	40	159	58	-	-	-	-	-	-	274
M10-A-17	155	16	801	81	-	-	-	-	-	-	985
					M5[+Fe]-NE						
M5-B-1	790	48	805	49	-	-	-	-	-	-	1642
M5-B-2	818	49	797	48	-	-	0.8	<0.1	0.4	<0.1	1664
M5-B-3	697	36	1092	56	1.7	0.1	1.7	0.1	2.6	0.1	1943
M5-B-4	496	35	825	58	-	-	1.7	0.1	-	-	1432
M5-B-5	210	19	803	73	1.9	0.2	0.9	0.1	-	-	1094
M5-B-6	100	25	280	70	-	-	-	-	-	-	400
M5-B-7	96	13	617	83	-	-	-	-	0.6	0.1	744
M5-B-8	37	12	268	85	-	-	-	-	-	-	314
M5-B-19*	305	11	2450	85	0.9	<0.1	-	-	-	-	2872
					M6[−Fe]-S						
M6-B-1	-	-	4449	80	4.1	<0.1	21	0.4	19	0.3	5560
M6-B-6	-	-	716	93	0.4	<0.1	1.2	0.2	1.0	0.1	768
Annual Fluxes	Flux	Percent	Flux	Percent	Flux	Percent	Flux	Percent	Flux	Percent	Flux
M10[+Fe]-N	72917	58	49978	40	9.1	<0.1	38	<0.1	-	-	125176
M5[+Fe]-NE	56856	28	135466	67	87	<0.1	97	<0.1	59	<0.1	203315
M6[−Fe]-S	-	-	68989	83	56	0.1	260	0.3	231	0.3	82659

[a]*Chaetoceros* included resting spores (*Phaeceros* and *Hyalochaete* varieties).
[b]*Dactyliosolen antarcticus* was often present as half frustules which were enumerated and divided by 2. Other than the species presented, centric diatom fluxes (mainly *Coscinodiscus* spp. and *Thalassiosira* spp.) were grouped and classified according to size.
[c]Hyphen indicates species was not detected.
[d]*Eucampia antarctica* var. *antarctica* were present almost exclusively as the winter growth stage, rare occurrences of vegetative cell were not quantified separately.
[e]Hyphen indicates species was not detected.

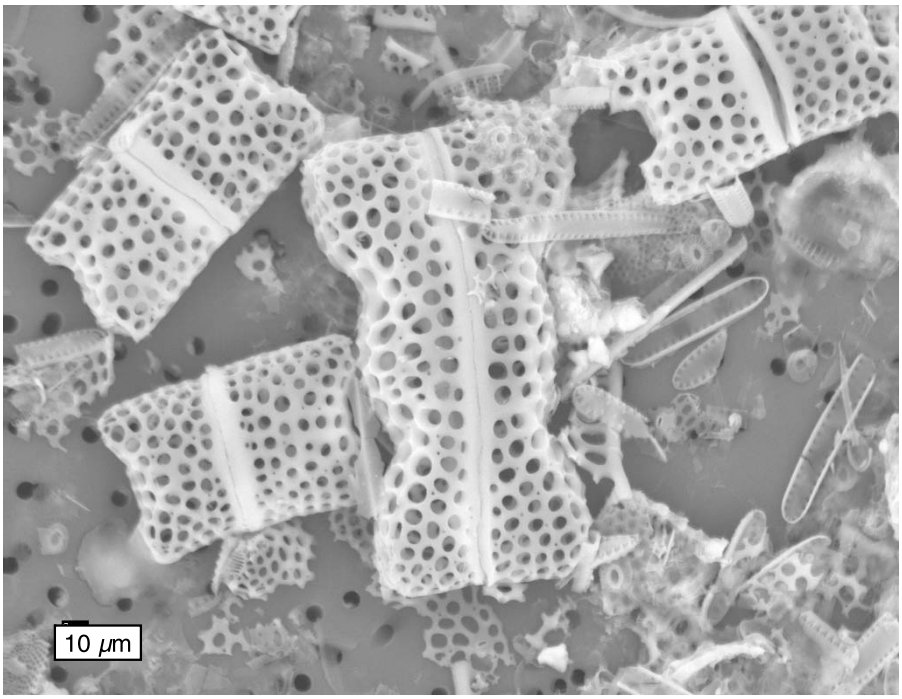

Figure 4. SEM imaging of sediment trap material from the [+Fe] environment showing the winter growth stage of *Eucampia antarctica* var. *antarctica*, identified by the uneven elevations on the frustules leading to the formation of coiling chains. Scale bar is 10 μm.

Table 2). The Si/C ratios were highest at the M6[−Fe]-S site with a range of 6.4 to 7.8 and lowest at the M10[+Fe]-N site with a range of 2.3–2.6; Si/C ratios at M5[+Fe]-NE were intermediate at 4.0–4.1 (Figure 3c). The relative differences observed for Si/N ratios between the sites were very similar to those described for Si/C, only the absolute values were an order of magnitude higher (Figure 3d and Table 2).

[31] For each of the three sediment trap sites we provide a range of annual export flux estimates together with the corresponding Si/C and Si/N ratios. Although we deemed it pertinent to extrapolate the first export flux measurement to estimate annual fluxes, it should be acknowledged that the differences resulting from the three extrapolation methods are minor compared to the major differences observed between the sediment trap sites (Figure 3). These small differences between the three methods are dependent on particle settling velocities estimated by comparing the propagation of chlorophyll and export signals or export signals at different sediment trap deployment depths (section 3.7). The only study to compare direct field measurements of mean particle settling velocities with signal propagation velocities is that of [*Armstrong et al.*, 2009], who found good agreement between the two when sediment trap export signals at different depths were used. Taking this study into account we consider that the values computed by comparison of trap signals (marked with an asterisk in Figure 3) are the most plausible estimates for annual fluxes and they are used in the following discussion.

4.4. Spatial Patterns of Diatom Export Fluxes

[32] Diatom fluxes at M10[+Fe]-N and M5[+Fe]-NE were dominated by *Eucampia antarctica* var. *antarctica* (Fryxell) and *Fragilariopsis kerguelensis* which taken together accounted for >92% of the total diatom cells enumerated in every sample (Table 3). The export fluxes of *E. ant.* var. *ant.* were higher at M10[+Fe]-N ranging from 111–1755 $\times$ 10^4 compared to 37–818 $\times$ 10^4 valves m^{-2} d^{-1} at M5[+Fe]-NE, which accounted for between 16–71% and 11–49% of the total diatom export assemblages, respectively (Table 3). *Fragilariopsis kerguelensis* was subordinate to *E. ant.* var. *ant*. at M10[+Fe]-N with fluxes ranging from 132–801 $\times$ 10^4 valves m^{-2} d^{-1} (Table 3). At M5[+Fe]-NE *F. kerguelensis* fluxes of 268–2450 $\times$ 10^4 valves m^{-2} d^{-1} were similar or slightly larger than corresponding *E. ant.* var. *ant.* fluxes (Table 3). A key observation at both M10[+Fe]-N and M5[+Fe]-NE was that the highest proportion and fluxes of *F. kerguelensis* occurred during the November-December flux event of 2005, coincident with the lowest proportion and among the lowest fluxes of *E. ant.* var. *ant.* (Table 3).

[33] At the M6[−Fe]-S site the diatom export assemblage was dominated by *F. kerguelensis* with daily fluxes enhanced over those at the [+Fe] sites, ranging from 716–4449 $\times$ 10^4 valves m^{-2} d^{-1} and accounting for 80–93% of the total diatom assemblage (Table 3). In contrast to M10[+Fe]-N and M5[+Fe]-NE, no *E. ant.* var. *ant.* cells were observed in the flux assemblage at M6[−Fe]-S. The export fluxes of large diatoms (>10,000 μm^3; [*Cornet-Barthaux et al.*, 2007]) such as *Corethron pennatum*, *Dactyliosolen antarcticus*, *Rhizosolenia* spp. and *Thalassiothrix antarctica* were enhanced at M6[−Fe]-S compared to those observed at M10[+Fe]-N and M5[+Fe]-NE (Table 3). Although the diatom flux data at M6[−Fe]-S are based on the analysis of only two sampling cups it is

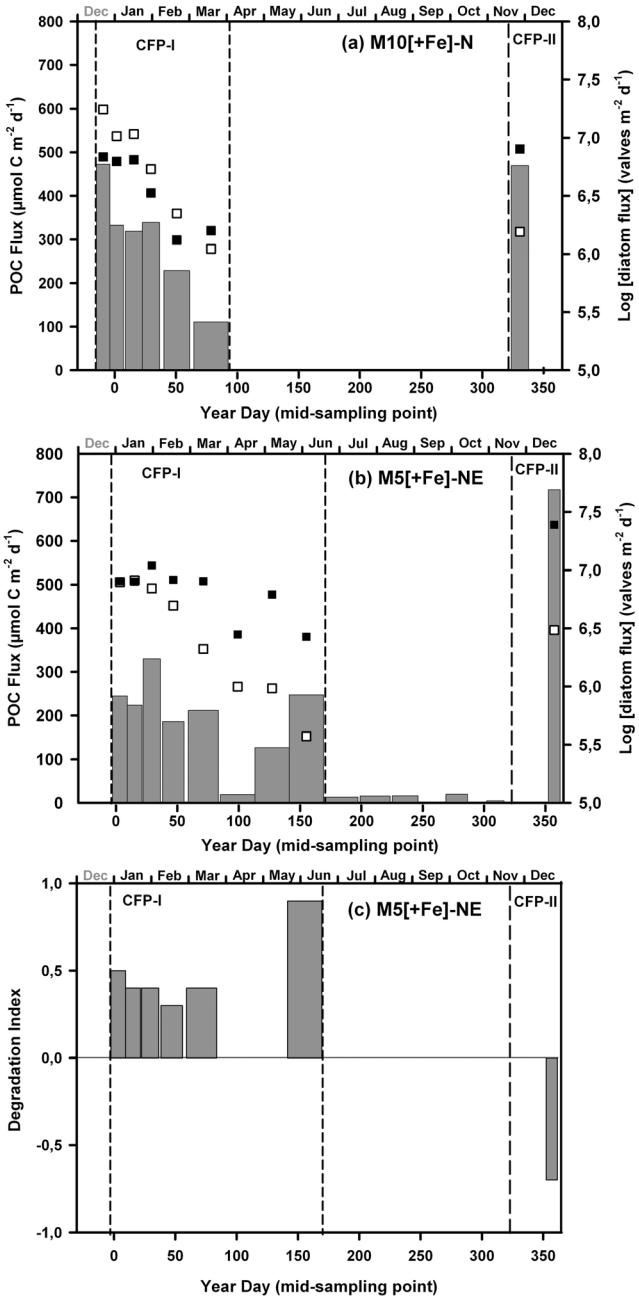

Figure 5. Particulate organic carbon flux (gray bars) and diatom fluxes (squares) at (a) M10[+Fe]-N and (b) M5[+Fe]-NE. White squares denote *E. ant*. var. *ant.* and black squares are *F. kerguelensis.* (c) Gray bars are amino acid based degradation index.

important to recognize that these two sampling events account for >91% of the annual POC flux (Table 1c).

4.5. Temporal Patterns of Diatom Export Fluxes in the +Fe Region

[34] In addition to the regime-specific (+Fe/−Fe) spatial comparisons, there were clear temporal trends present in the dominant diatom export assemblages at the [+Fe] sites, notably those of *E. ant.* var. *ant.* and *F. kerguelensis* (Table 3). At M10[+Fe]-N the export flux of *E. ant.* var. *ant.* decreased over the initial period of observation (year day 0–100), coinciding with a general decrease in POC flux (Figure 5a). Similarly at M5[+Fe]-NE *E. ant.* var. *ant.* export fluxes decreased gradually over the initial period of observation year day (0–150), although the corresponding decrease in POC flux was less obvious (Figure 5b). In contrast *F. kerguelensis* export fluxes were relatively constant for the first 40 and 90 days of observation at M10[+Fe]-N and M5[+Fe]-NE, respectively, after which they gradually declined (Figures 5a and 5b).

[35] The timing and magnitude of *E. ant.* var. *ant.* and *F. kerguelensis* export fluxes prompted the qualitative designation of two different flux periods to describe the dataset. Carbon Flux Period-I (CFP-I) covers the first period of observation day 0–100 at M10[+Fe]-N and days 0–150 at M5[+Fe]-NE) subsequent to the 2004 bloom and where *E. ant.* var. *ant.* fluxes gradually decline. Carbon Flux Period-II (CFP-II) covers the first export flux events of the 2005 bloom (cf. Figure 2) characterized by the highest POC fluxes at the respective sites and where generally speaking *E. ant.* var. *ant*. fluxes are lower and *F. kerguelensis* fluxes higher than those observed during CFP-I (Figure 5). Integrating the data from both the M10[+Fe]-N and M5[+Fe]-NE sites reveals a strong linear relationship ($R = 0.83$, $P = 0.05$, $n = 12$) between the flux of *E. ant.* var. *ant.* and POC during CFP-I (Figure 6a). At both [+Fe] sites the data points which deviate from this regression correspond to those occurring during CFP-II. Positive, although statistically weaker, correlations with POC flux were observed for *F. kerguelensis* ($R = 0.36$, $P = 0.53$, $n = 12$) and *C. pennatum* ($R = 0.72$, $P = 0.24$, $n = 12$) (Figures 6b and 6c) during CFP-I.

4.6. Biochemical Characteristics of Particulate Organic Matter

[36] The amino acid composition of selected sediment trap samples from M5[+Fe]-NE were determined and used to calculate the degradation index (DI) (equation (1)) of organic carbon in exported material (Figure 5c). Positive degradation index (DI)-values are indicative of fresh organic matter whilst negative values are characteristic of organic matter significantly altered by heterotrophic reworking [*Dauwe et al.*, 1999]. The resulting DI values from CFP-I were remarkably consistent at 0.4 ± 0.07 ($n = 5$). A sample analyzed (M5-B-8) was slightly higher at 0.9 (Figure 5c and Tables 1a–1c). In contrast the carbon exported during CFP-II at M5[+Fe]-NE had a negative DI-value of −0.7.

5. Discussion

[37] The three sediment trap locations M10[+Fe]-N, M5[+Fe]-NE, and M6[−Fe]-S are distinguished by contrasting diatom export assemblages, POC fluxes and Si/C and Si/N ratios. Overall, these differences are consistent with the M10[+Fe]-N trap (lowest Si/C ratios, highest *E. ant.* var. *ant.* fluxes) sampling the end-member naturally fertilized bloom and the M5[+Fe]-NE trap sampling an admixture of bloom material advected west and material from the less productive directly overlying waters (intermediate Si/C ratios and moderate *E. ant.* var. *ant.* fluxes) (cf. Figure 1). The M6[−Fe]-S trap samples the end member HNLC waters (highest Si/C ratios, zero *E. ant.* var. *ant.* fluxes).

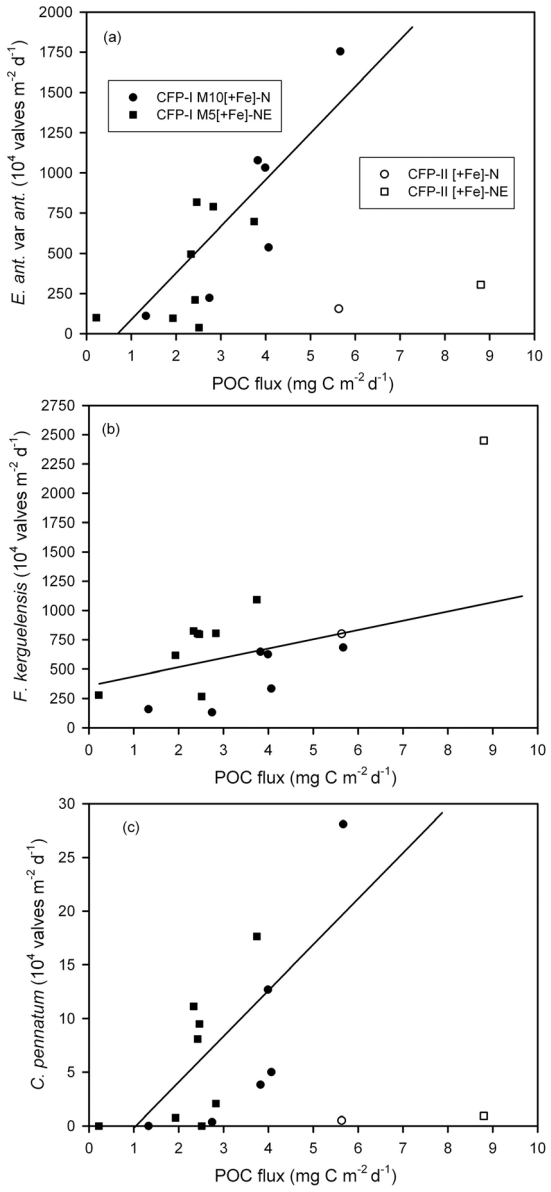

Figure 6. Relationship between fluxes of (a) *E. antarctica* var. *antarctica*, (b) *F. kerguelensis*, and (c) *C. pennatum* with POC at M10[+Fe]-N and M5[+Fe]-NE. The black and white symbols are from carbon flux phases one (CFP-I) and two (CFP-II) as identified in Figure 5. Circles are from M10[+Fe]-N and squares are from M5[+Fe]-NE. Solid black lines are linear regressions for CFP-I samples. Regression statistics are R = 0.83, n = 12, P < 0.05 for *E. ant.* var. *ant.* (Figure 6a) R = 0.36, n = 12, P < 0.05 for *F. kerguelensis* (Figure 6b) and R = 0.72, n = 12, P < 0.05 for *C. pennatum* (Figure 6c).

5.1. Diatom Export Assemblage and Elemental Fluxes

5.1.1. The [–Fe] Region: *Fragilariopsis kerguelensis* and Large Diatoms

[38] Diatom fluxes at M6[−Fe]-S were numerically dominated (>80%) by *F. kerguelensis*. In addition several large diatom species (biovolume >10,000 μm^3 [*Cornet-Barthaux et al.*, 2007]), were important components of the export flux assemblage (Table 3). Although these large species, *C. pennatum, D. antarcticus*, *Rhizosolenia* spp. and *T. antarctica* accounted for only 5% of total valves enumerated, they are more than an order of magnitude larger than *F. kerguelensis* [*Cornet-Barthaux et al.*, 2007] so that their potential contribution to total POC fluxes may have been of the order of 30%. A particularly striking observation was that the annual fluxes of *C. pennatum* and *Rhizosolenia* spp. were significantly enhanced at M6[−Fe]-S by factors of 2.4–6.8 relative to the M10[+Fe]-N and M5[+Fe]-NE sites (Table 3). The diatom export flux data at M6[−Fe]-S is consistent with contemporaneous water column studies at the same site which found that *F. kerguelensis*, *C. pennatum*, and *D. antarcticus* were important components of a phytoplankton community [*Poulton et al.*, 2007], in which microphytoplankton (>20 μm) accounted for 46 ± 12% of euphotic layer-integrated production [*Seeyave et al.*, 2007]. The dominance of the medium-sized *F. kerguelensis* and larger *C. pennatum*, *D. antarcticus* and *Rhizosolenia* spp. for export at M6[−Fe]-S is consistent with previous syntheses that have highlighted the role of grazing pressure in the iron-limited Southern Ocean for the preferential accumulation of such large and heavily silicified diatoms that drive the silicon pump in a "high opal – low carbon" flux regime [*Smetacek et al.*, 2004].

5.1.2. The +Fe Region: *Eucampia antarctica* var. *antarctica*

[39] At both M10[+Fe]-N and M5[+Fe]-NE sites *E. ant.* var. *ant.* valves were an important component of the diatom flux assemblage, accounting for up to 71% of the total diatom assemblage at M10[+Fe]-N (Table 3). In contrast, *E. ant.* var. *ant.* was entirely absent in the M6[−Fe]-S flux assemblage (Table 3), consistent with their absence from water-column measurements in the [−Fe] region [*Poulton et al.*, 2007]. The export fluxes of *E. ant.* var. *ant.* were highest during carbon flux period-I (CFP-I) (Figure 5). *Fragilariopsis kerguelensis* was also an important component of the diatom flux assemblage during CFP-I at M10[+Fe]-N and M5[+Fe]-NE. At both [+Fe] sites the difference between *E. ant.* var. *ant.* and *F. kerguelensis* fluxes narrowed as CFP-I progressed, in line with a general decrease in POC fluxes (Figures 5a and 5b). This effect was more pronounced at M5[+Fe]-NE and *F. kerguelensis* fluxes exceeded *E. ant* var. *ant.* fluxes during the latter part of CFP-I, probably due to the influence of the less productive waters directly overlying the sediment trap location (Figure 1). The highest fluxes of *F. kerguelensis*, and largest differences compared to *E. ant.* var. *ant* fluxes, occurred during CFP-II in November/December 2005 (Figure 5).

[40] Evidence of reproduction in the resting spores of *E. ant.* var. *ant.* and *E. antarctica* var. *recta* (ice-edge form) has led them to be regarded as winter growth stages [*Fryxell and Prasad*, 1990]. Practically the entire assemblage of *E. ant.* var. *ant.* valves enumerated in our samples comprised the heavily silicified resting spores (or winter growth stages) (Figure 4). The rare occurrence of vegetative stages were not quantified (see methods). Considering the export flux data from both [+Fe] sites during CFP-I, a significant linear relationship was found between POC and *E. ant.* var. *ant.*-winter growth stage (WGS) fluxes (Figure 6a). At M10[+Fe]-N and M5[+Fe]-NE, the data

points that significantly deviate from the derived correlation correspond to carbon flux period-II (CFP-II) occurring in November–December 2005 (Figure 6a). The export fluxes of *F. kerguelensis* and *C. pennatum* also displayed positive, although statistically weaker, relationships with POC flux during CFP-I (Figures 6b and 6c). Although the carbon content of *C. pennatum* cells is around 3–5 times larger than that of *E. ant*. var. *ant.* [*Cornet-Barthaux et al.*, 2007], their absolute fluxes during CFP-I were on the order of 80 times lower (Table 3 and Figure 6). The overall finding that *E. ant* var. *ant.*-WGS fluxes dominate the diatom contribution to total POC flux in the [+Fe] region is consistent with shallow (250 m) sediment trap deployments in the [+Fe] region north of the Crozet plateau that showed high carbon flux and export ratios associated with an *E. ant.* var. *ant.* dominated export assemblage [*Salter et al.*, 2007].

5.1.3. Evidence From Organic Matter Degradation for Efficiency of POC Flux

[41] The variation in the amino acid composition of settling particles from M5[+Fe]-NE was assessed using principal components analysis to quantify differences in the degradation state (DI) of organic matter. Changes in the amino acid composition of settling particles occur as a function of depth due to degradation of material as it sinks through the water column [*Lee et al.*, 2000]. Consequently we restricted our amino acid analysis to trap material from M5[+Fe]-NE (deployed at 3195 m) to enable comparison with a larger data-set acquired from 3000 m in the Northeast Atlantic [*Salter et al.*, 2010].

[42] The amino acid analyses are based on a limited number of samples and therefore must be interpreted with an element of caution. Taking these limitations into account, the DI-values available independently support the notion of two major flux phases in the [+Fe] region (Figure 5), but the nature of the transition between CFP-II and CFP-I is difficult to ascertain. Although CFP-II only has one sample, it is drastically different from the remainder of the data-set (Figure 5c), but is in fact more consistent with the negative DI-values generally observed in sediment trap material exported to 3000 m elsewhere—e.g., in the North Atlantic [*Salter et al.*, 2010]. The positive DI-values measured during CFP-I are more intriguing since they are similar to the values observed for undegraded phytoplankton [*Dauwe et al.*, 1999]. Given the quantitative importance of *E. ant.* var. *ant.* during CFP-I (Figures 5 and 6a) suggests that the export of viable winter growth stages of *E. ant.* var. *ant.* to be the dominant mechanism of POC export from the [+Fe] region.

5.1.4. Summary: Role of *Eucampia antarctica* var. *antarctica* Ecology in POC Flux

[43] The importance of *E. ant.* var. *ant.* export fluxes at M10[+Fe]-N and M5[+Fe]-NE and complete absence at M6 [−Fe]-S imply that this species thrives in high-iron environments in proximity to island habitats. Further, the export of *E. ant.* var. *ant.* winter growth stages appears to be an important driver of the enhanced deep-water carbon export (Figure 3a) attributed to natural iron fertilization of HNLC waters [*Pollard et al.*, 2009; *Salter*, 2008]. Comparative sediment trap data from other analogous Southern Ocean island systems is lacking. However, plankton surveys and data from sediments show that part of the wider distribution of *E. antarctica* is related to dispersal from zones of iron-fertilized production closely linked with ocean island systems, including South Georgia [*Korb et al.*, 2008] and Kerguelen [*Armand et al.*, 2008a].

[44] Rapid growth responses under favorable conditions and strategies for maintaining persistence in regions where such conditions occur are both advantageous traits for bloom species [*Smetacek*, 1985]. Consistent with the first of these characteristics, *E. antarctica* displayed the strongest growth response within bioassay experiments conducted in [+Fe] waters north of the Crozet Plateau [*Moore et al.*, 2007b]. The common ecological strategy of resting spore/winter growth stage formation can facilitate rapid sinking of viable cells to the benthos or deeper strata of the water column, which can then act as an overwintering refuge [*Smetacek*, 1985]. The majority fate of sinking cells may still be mortality [*Smetacek*, 1985; *Walsh*, 1983] and indeed those observed to be sinking past depths >2000 m off the plateau will clearly not be returned to the surface the following spring. However, the retention of even a small proportion of cells over the plateau would maintain a seed stock within the region of enhanced iron availability the following spring. Winter-growth stages also differ from resting spores in that they can reproduce and hence may further increase seeding stock during the turbulent winter months [*Fryxell*, 1994].

[45] Since nitrate concentrations were non-limiting (18 μM) [*Sanders et al.*, 2007] low dissolved iron [*Planquette et al.*, 2007] and orthosilicate concentrations [*Salter et al.*, 2007] are plausible triggers for winter growth stage formation at Crozet, with strong evidence for *in-situ* Fe stress in the declining stages of the bloom for the +Fe area [*Moore et al.*, 2007b]. We thus suggest that a rapid response to enhanced iron [*Moore et al.*, 2007a], followed by sedimentation of winter resting stages following iron depletion, are both entirely consistent with the life-cycles which bloom forming Southern Ocean diatoms would be expected to evolve [*Smetacek*, 1985; *Smetacek et al.*, 2004]. The ecological strategy of *E. ant* var. *ant.* winter growth stage formation thus appears to combine with lateral off-shore transport of a large proportion of the population to increase the strength of the biological carbon pump around the Crozet Islands.

5.2. Importance of Diatom Export Assemblages for Annual Export Fluxes, Si/C and Si/N Ratios

[46] The annual Si/C and Si/N export ratios of deep-ocean particle flux increased by a factor 3.5 when moving away from a naturally Fe-fertilized end-member M10[+Fe]-N, through a transitional site M5[+Fe]-NE, to an iron-deplete HNLC-type end member M6[−Fe]-S (Figures 3c and 3d). These changes in export ratios were caused by increases in C and N fluxes, rather than changes in BSi fluxes which were relatively similar (<15% CV) between the three study sites (Figure 3 and Table 2). The Si/C ratio of 7.8 at M6[−Fe]-S is similar to that previously reported in deep-sediment traps in the Southern Ocean (10.4 at 4023 m), whilst the much lower value of 2.3 at M10[+Fe]-N is more comparable to Si/C ratios for export at 200 m (2.6) [*Ragueneau et al.*, 2002]. The large differences between the [+Fe] and [−Fe] regimes indicates that in our study area the decoupling of Si export from C and N export to the deep-ocean is driven by iron availability. The established physiological response of diatoms to iron supply [*Coale et al.*, 2004; *Franck et al.*, 2000] and resulting Si/N cell quotas [*Hutchins and*

Bruland, 1998; *Takeda*, 1998] are consistent with our observed Si/C and Si/N ratios (Figures 3c and 3d). Large differences in diatom export assemblages and transitions observed between the [+Fe] and [−Fe] sites (Table 3) suggest diatom species composition may amplify these physiological effects when considering the Si/C and Si/N ratios of particulate material exported to the deep-ocean.

[47] At the M6[−Fe]-S site, iron limitation appears to favor the ecological selection of large heavily-armored diatoms such as *C. pennatum, D. antarcticus* and the heavily-silicified *F. kerguelensis* (Table 3). Although sub-optimal iron concentrations can limit the growth rate of large diatoms [*Moore et al.*, 2007a] they are postulated to accumulate biomass in HNLC regions through resistance to grazing losses [*Smetacek et al.*, 2004]. The rapid export of large frustules of *C. pennatum* and *D. antarcticus*, which were frequently observed as empty frustules in the surface ocean [*Poulton et al.*, 2007] and those of *F. kerguelensis* (Table 3) leads to preferential BSi export resulting in the large Si/C and Si/N ratios observed at M6[−Fe]-S (Figures 3c and 3d).

[48] At M10[+Fe]-N diatom export assemblages were dominated by *E. ant.* var. *ant*. winter growth stages. As argued above, the proximity to a topography-derived Fe source [*Planquette et al.*, 2007] at M10[+Fe]-N clearly favors *E. ant.* var. *ant.* populations. The strategy of winter growth stage formation by *E. ant.* var. *ant*. results in the export of carbon-rich frustules characterized by the low Si/C and Si/N export ratios observed at M10[+Fe]-N (Figures 3c and 3d). The role of diatom export assemblages on Si/C and Si/N export ratios is supported by data from the M5[+Fe]-NE site where the sediment trap was deployed slightly away from the influence of the Fe-fertilized island region (Figure 1). The diatom export assemblage at M5[+Fe]-NE retains to a smaller extent the *E. ant.* var. *ant.* export signal of the M10[+Fe]-N site whilst displaying intermediate fluxes of the large diatoms *C. coretheron* and *D. antarcticus* (Table 3) and enhanced fluxes of *F. kerguelensis* characteristic of the M6[−Fe]-S site. The admixture of diatom export assemblages at M5[+Fe]-NE is reflected in Si/C and Si/N export ratios which fall between the M10[+Fe]-N and M6 [−Fe]-S end-members, although they are more similar to the M10[+Fe]-N site (Figures 3c and 3d). The export flux data from our study area shows how the availability of iron can shape the diatom community structure through a balance of resource and grazing controls which in turn controls diatom export assemblages that establish the nutrient stoichiometry of the biological pump.

5.3. Contrast Between Diatom Species in Antarctic Open Ocean and Ocean Island Iron-Fertilized Blooms and Implications for Export Flux

[49] Mesoscale iron addition experiments (AFeXs) in the Southern Ocean induced blooms which were largely dominated by the open ocean diatoms *F. kerguelensis* and *Pseudo-nitzschia* spp [*de Baar et al.*, 2005]. In contrast phytoplankton blooms associated with two natural fertilization experiments (NFeXs) in the Southern Ocean (KEOPS and CROZeX) indicated the importance of *Chaetoceros spp* and *E. ant.* var. *ant.* and their resting spores/winter growth stages [*Armand et al.*, 2008a; *Poulton et al.*, 2007]. It would appear that the different diatom bloom communities in AFeXs and NFeXs may primarily reflect the proximity to shallow topography and hence the presence of diatom seed populations, in addition to a natural supply of iron. Support for this inference is provided by data from other naturally Fe-rich waters such as the polar frontal jet where, in the absence of proximity to shallow topography, *F. kerguelensis* [*de Baar et al.*, 1995] and blooms of *Corethron* spp. occur [*Bathmann et al.*, 1997]. Additionally, the massive bloom induced by an AFeX in the Western sub-arctic Pacific (SEEDS) was dominated by *Chaetoceros debilis*; which apparently originated from the coastal areas of the Kuril and Aleutian Islands [*Tsuda et al.*, 2003]. Based on available data it seems that island-system NFeXs are characterized by the response of diatoms represented in localized seed populations whereas open Southern Ocean AFeXs blooms are dominated by oceanic diatoms including *F. kerguelensis* and *Pseudo-nitzschia* spp.

[50] *Eucampia antarctica* var. *antarctica* and Hyalochaete *Chaetoceros* spp differ from *F. kerguelensis* and *Pseudo-nitzschia* in forming heavily-silicified resting spores/winter growth stages with winter growth stages an important component of flux from the Fe-fertilized bloom area to the North of the Crozet Islands (Figure 6a). *Eucampia antarctica* var. *antarctica* winter growth stages and Hyalochaete *Chaetoceros* spp were also an important feature of surface-water [*Armand et al.*, 2008a] and surface-sediment assemblages [*Armand et al.*, 2008b] in the Fe-fertilized region of the Kerguelen bloom. The enhanced carbon export reported from the Crozet Island system [*Pollard et al.*, 2009; *Salter*, 2008] and Kerguelen [*Blain et al.*, 2007] may thus represent a biogeochemical response which results not simply from enhanced iron supply, but rather from the combined response of diatoms from island seeding points to a favorable growth (iron rich) environment and the subsequent formation of resting spores/winter growth stages that are especially efficient at carbon export. Consequently the carbon flux estimates, and C:Fe sequestration efficiencies calculated from NFeXs [*Blain et al.*, 2007; *Pollard et al.*, 2009] may be considered as highly specific to the island systems chosen as “natural iron laboratories”. Such environments may therefore not provide accurate analogs for the way the biological carbon pump would respond to enhanced iron supply in open ACC waters dominated by diatoms with different life-cycle strategies.

6. Conclusion

[51] We have analyzed diatom export assemblages and biogeochemical properties of settling particulate material from the [+Fe] productivity regime of a naturally fertilized island system in the Southern Ocean and an adjacent and [−Fe] HNLC control area. The enhanced carbon fluxes measured in response to natural iron fertilization were tightly correlated ($R = 0.83$, $n = 12$, $P < 0.05$) with the resting spore (winter growth stage) export of a single diatom species, *Eucampia antarctica* var. *antarctica*. An amino acid-based index of organic matter degradation indicated an unusually well preserved state of the *Eucampia*-associated organic matter flux, likely influenced by the ecology of resting spores that are adapted to settle rapidly out of the surface ocean, preserving viable cells. Export fluxes in the [−Fe] control study area were dominated by F. kerguelensis and large, heavily silicified diatoms; *C. pennatum, D. antarcticus*,

Rhizosolenia spp. and *T. antarctica*. Consequently, although organic carbon fluxes were enhanced under [+Fe] conditions, BSi fluxes were comparable between the [+Fe] and [−Fe] study areas leading to 2.0–3.4-fold higher Si/C and 2.2–3.5 fold higher Si/N export ratios under iron deplete conditions. Taken together the results demonstrate that the availability of iron can shape the diatom community structure through a balance of resource and grazing controls which in turn controls diatom export assemblages that establish the nutrient stoichiometry of the biological pump. The contribution of *Eucampia*-resting spore (winter growth stage) ecology to the enhanced carbon export measured during this natural iron fertilization experiment indicates a very specific response of the biological carbon pump close to island systems. More generally our results emphasize the need for a species-centered approach to the understanding of biogeochemical fluxes.

[52] **Acknowledgments.** The research was joint-funded by the NERC core strategic program, Biophysical Interactions and Controls on Export Production (BICEP), and the lead author's NERC studentship, NER/S/A/2003/11855. We would like to thank the captain and the crew of R.R.S. *Discovery* on cruises D285, D286, and D300. We are grateful to all of the CROZEX participants, Hugh Venables for his assistance in processing remote-sensing data and Alex Poulton for phytoplankton counts. Leanne Armand contributed useful discussions on *Eucampia*.

References

Armand, L. K., et al. (2008a), Late summer diatom biomass and community structure on and around the naturally iron-fertilized Kerguelen Plateau in the Southern Ocean, *Deep Sea Res., Part II*, *55*(5–7), 653–676, doi:10.1016/j.dsr2.2007.12.031.

Armand, L. K., et al. (2008b), Diatoms preserved in surface sediments of the north-eastern Kerguelen Plateau, *Deep Sea Res., Part II*, *55*(5–7), 677–692, doi:10.1016/j.dsr2.2007.12.032.

Armstrong, R. A., et al. (2009), Settling velocity spectra and the ballast ratio hypothesis, *Deep Sea Res., Part II*, *56*(18), 1470–1478, doi:10.1016/j.dsr2.2008.11.032.

Assmy, P., et al. (2007), Mechanisms determining species dominance in a phytoplankton bloom induced by the iron fertilization experiment EisenEx in the Southern Ocean, *Deep Sea Res., Part I*, *54*(3), 340–362, doi:10.1016/j.dsr.2006.12.005.

Baines, S. B., B. S. Twining, M. A. Brzezinski, D. M. Nelson, and N. S. Fisher (2010), Causes and biogeochemical implications of regional differences in silicification of marine diatoms, *Global Biogeochem. Cycles*, *24*, GB4031, doi:10.1029/2010GB003856.

Bathmann, U. V., R. Scharek, C. Klaas, C. D. Dubischar, and V. Smetacek (1997), Spring development of phytoplankton biomass and composition in major water masses of the Atlantic sector of the Southern Ocean, *Deep Sea Res., Part II*, *44*(1–2), 51–67.

Blain, S., et al. (2007), Effect of natural iron fertilization on carbon sequestration in the Southern Ocean, *Nature*, *446*(7139), 1070–1071, doi:10.1038/nature05700.

Boyd, P. W., et al. (2000), A mesoscale phytoplankton bloom in the polar Southern Ocean stimulated by iron fertilization, *Nature*, *407*(6805), 695–702, doi:10.1038/35037500.

Buesseler, K. O., et al. (2005), Particle export during the southern ocean iron experiment (SOFeX), *Limnol. Oceanogr.*, *50*(1), 311–327, doi:10.4319/lo.2005.50.1.0311.

Burckle, L. H. (1984), Ecology and paleoecology of the marine diatom *Eucampia antarctica* (Castr.) Mangin, *Mar. Micropaleontol.*, *9*(1), 77–86, doi:10.1016/0377-8398(84)90024-0.

Coale, K. H., et al. (2004), Southern ocean iron enrichment experiment: Carbon cycling in high- and low-Si waters, *Science*, *304*(5669), 408–414, doi:10.1126/science.1089778.

Conley, D. J. (1998), An interlaboratory comparison for the measurement of biogenic silica in sediments, *Mar. Chem.*, *63*(1–2), 39–48, doi:10.1016/S0304-4203(98)00049-8.

Cornet-Barthaux, V., et al. (2007), Biovolume and biomass estimates of key diatoms in the Southern Ocean, *Aquat. Microb. Ecol.*, *48*(3), 295–308, doi:10.3354/ame048295.

Cowie, G. L., and J. I. Hedges (1992), Improved amino acid quantification in environmental samples: Charge-matched recovery standards and reduced analysis time, *Mar. Chem.*, *37*(3–4), 223–238, doi:10.1016/0304-4203(92)90079-P.

Dauwe, B., et al. (1999), Linking diagenetic alteration of amino acids and bulk organic matter reactivity, *Limnol. Oceanogr.*, *44*(7), 1809–1814, doi:10.4319/lo.1999.44.7.1809.

de Baar, H. J. W., et al. (1995), Importance of iron for plankton blooms and carbon dioxide drawdown in the Southern Ocean, *Nature*, *373*(6513), 412–415, doi:10.1038/373412a0.

de Baar, H. J. W., et al. (2005), Synthesis of iron fertilization experiments: From the Iron Age in the Age of Enlightenment, *J. Geophys. Res.*, *110*, C09S16, doi:10.1029/2004JC002601.

Fabres, J., et al. (2002), Composition and spatio-temporal variability of particle fluxes in the western Alboran Gyre, Mediterranean Sea, *J. Mar. Syst.*, *33*, 431–456, doi:10.1016/S0924-7963(02)00070-2.

Franck, V. M., et al. (2000), Iron and silicic acid concentrations regulate Si uptake north and south of the Polar Frontal Zone in the Pacific Sector of the Southern Ocean, *Deep Sea Res., Part II*, *47*(15–16), 3315–3338, doi:10.1016/S0967-0645(00)00070-9.

Froneman, P. W., et al. (1997), Microphytoplankton assemblages in the waters surrounding South Georgia, Antarctica during austral summer 1994, *Polar Biol.*, *17*(6), 515–522, doi:10.1007/s003000050150.

Fryxell, G. A. (1991), Comparison of winter and summer growth stages of the diatom *Eucampia antarctica* from the Kerguelen Plateau and South of the Antarctic Convergence Zone, *Proc. Ocean Drill. Program Sci. Results*, *119*, 675–685.

Fryxell, G. A. (1994), Planktonic marine diatom winter stages: Antarctic alternatives to resting spores, in *Proceedings of the 11th International Diatom Symposium*, edited by J. P. Kociolek, pp. 437–448, Calif. Acad. of Sci., San Francisco, Calif.

Fryxell, G. A., and A. Prasad (1990), *Eucampia antarctica* var. *recta* (Mangin) stat. nov. (Biddulphiaceae, Bacillariophyceae): Life stages at the Weddell Sea ice edge, *Phycologia*, *29*(1), 27–38, doi:10.2216/i0031-8884-29-1-27.1.

Gupta, L. P., and H. Kawahata (2000), Amino acid and hexosamine composition and flux of sinking particulate matter in the equatorial Pacific at 175°E longitude, *Deep Sea Res., Part I*, *47*(10), 1937–1960, doi:10.1016/S0967-0637(00)00009-1.

Hoffmann, L. J., I. Peeken, K. Lochte, P. Assmy, and M. Veldhuis (2006), Different reactions of Southern Ocean phytoplankton size classes to iron fertilization, *Limnol. Oceanogr.*, *51*(3), 1217–1229, doi:10.4319/lo.2006.51.3.1217.

Hutchins, D. A., and K. W. Bruland (1998), Iron-limited diatom growth and Si : N uptake ratios in a coastal upwelling regime, *Nature*, *393*(6685), 561–564, doi:10.1038/31203.

Ingalls, A. E., et al. (2006), Seasonal trends in the pigment and amino acid compositions of sinking particles in biogenic $CaCO_3$ and SiO_2 dominated regions of the Pacific sector of the Southern Ocean along 170°W, *Deep Sea Res., Part I*, *53*(5), 836–859, doi:10.1016/j.dsr.2006.01.004.

Korb, R. E., M. J. Whitehouse, A. Atkinson, and S. E. Thorpe (2008), Magnitude and maintenance of the phytoplankton bloom at South Georgia: A naturally iron-replete environment, *Mar. Ecol. Prog. Ser.*, *368*, 75–91, doi:10.3354/meps07525.

Lee, C., et al. (2000), Composition and flux of particulate amino acids and chloropigments in equatorial Pacific seawater and sediments, *Deep Sea Res., Part I*, *47*(8), 1535–1568, doi:10.1016/S0967-0637(99)00116-8.

Lindroth, P., and K. Mopper (1979), High-performance liquid-chromatographic determination of sub-picomole amounts of amino acids by pre-column fluorescence derivatization with ortho-Phthaldialdehyde, *Anal. Chem.*, *51*(11), 1667–1674, doi:10.1021/ac50047a019.

Marinov, I., M. Follows, A. Gnanadesikan, J. L. Sarmiento, and R. D. Slater (2008a), How does ocean biology affect atmospheric pCO_2? Theory and models, *J. Geophys. Res.*, *113*, C07032, doi:10.1029/2007JC004598.

Marinov, I., A. Gnanadesikan, J. L. Sarmiento, J. R. Toggweiler, M. Follows, and B. K. Mignone (2008b), Impact of oceanic circulation on biological carbon storage in the ocean and atmospheric pCO_2, *Global Biogeochem. Cycles*, *22*, GB3007, doi:10.1029/2007GB002958.

Martin, J. H. (1990), Glacial-interglacial CO_2 change: The Iron Hypothesis, *Paleoceanography*, *5*(1), 1–13, doi:10.1029/PA005i001p00001.

Moore, C. M., et al. (2007a), Iron-light interactions during the CROZet natural iron bloom and EXport experiment (CROZEX): II—Taxonomic responses and elemental stoichiometry, *Deep Sea Res., Part II*, *54*(18–20), 2066–2084, doi:10.1016/j.dsr2.2007.06.015.

Moore, C. M., et al. (2007b), Iron-light interactions during the CROZet natural iron bloom and EXport experiment (CROZEX) I: Phytoplankton growth and photophysiology, *Deep Sea Res., Part II*, *54*(18–20), 2045–2065, doi:10.1016/j.dsr2.2007.06.011.

Moore, J. K., and M. R. Abbott (2002), Surface chlorophyll concentrations in relation to the Antarctic Polar Front: Seasonal and spatial patterns from satellite observations, *J. Mar. Syst.*, *37*(1–3), 69–86, doi:10.1016/S0924-7963(02)00196-3.

Mortlock, R. A., and P. N. Froelich (1989), A simple method for the rapid determination of biogenic opal in pelagic marine-sediments, *Deep Sea Res., Part A*, *36*(9), 1415–1426, doi:10.1016/0198-0149(89)90092-7.

Nieuwenhuize, J., et al. (1994), Rapid analysis of organic carbon and nitrogen in particulate materials, *Mar. Chem.*, *45*(3), 217–224, doi:10.1016/0304-4203(94)90005-1.

Nodder, S. D., M. A. Charette, A. M. Waite, T. W. Trull, P. W. Boyd, J. Zeldis, and K. O. Buesseler (2001), Particle transformations and export flux during an *in situ* iron-stimulated algal bloom in the Southern Ocean, *Geophys. Res. Lett.*, *28*(12), 2409–2412, doi:10.1029/2001GL013008.

Planquette, H., et al. (2007), Dissolved iron in the vicinity of the Crozet Islands, Southern Ocean, *Deep Sea Res., Part II*, *54*(18–20), 1999–2019, doi:10.1016/j.dsr2.2007.06.019.

Pollard, R., et al. (2007), The CROZet natural iron bloom and EXport experiment (CROZEX), *Deep Sea Res., Part II*, *54*(18–20), 1905–1914, doi:10.1016/j.dsr2.2007.07.023.

Pollard, R. T., et al. (2009), Southern Ocean deep-water carbon export enhanced by natural iron fertilization, *Nature*, *457*(7229), 577–580, doi:10.1038/nature07716.

Poulton, A. J., et al. (2007), Phytoplankton community composition around the Crozet Plateau, with emphasis on diatoms and Phaeocystis, *Deep Sea Res., Part II*, *54*(18–20), 2085–2105, doi:10.1016/j.dsr2.2007.06.005.

Priddle, J., and G. Fryxell (1985), *Handbook of Common Plankton Diatoms in the Southern Ocean: Centrales Except the Genus Thalassiosira*, 158 pp., Br. Antarct. Surv., Cambridge, U. K.

Ragueneau, O., et al. (2002), Si/C decoupling in the world ocean: is the Southern Ocean different? *Deep Sea Res., Part II*, *49*(16), 3127–3154, doi:10.1016/S0967-0645(02)00075-9.

Ragueneau, O., S. Schultes, K. Bidle, P. Claquin, and B. Moriceau (2006), Si and C interactions in the world ocean: Importance of ecological processes and implications for the role of diatoms in the biological pump, *Global Biogeochem. Cycles*, *20*, GB4S02, doi:10.1029/2006GB002688.

Salter, I. (2008), *Particle Flux in the North-east Atlantic and Southern Ocean*, Ph.D. thesis, 339 pp., Sch. of Ocean and Earth Sci., Univ. of Southampton, Southampton, U. K.

Salter, I., et al. (2007), Estimating carbon, silica and diatom export from a naturally fertilized phytoplankton bloom in the Southern Ocean using PELAGRA: A novel drifting sediment trap, *Deep Sea Res., Part II*, *54* (18–20), 2233–2259, doi:10.1016/j.dsr2.2007.06.008.

Salter, I., et al. (2010), The association between biogenic and inorganic minerals and the amino acid composition of settling particles, *Limnol. Oceanogr.*, *55*(5), 2207–2218, doi:10.4319/lo.2010.55.5.2207.

Sanders, R., et al. (2007), New production and the *f* ratio around the Crozet Plateau in austral summer 2004–2005 diagnosed from seasonal changes in inorganic nutrient levels, *Deep Sea Res., Part II*, *54*(18–20), 2191–2207, doi:10.1016/j.dsr2.2007.06.007.

Seeyave, S., et al. (2007), Phytoplankton productivity and community structure in the vicinity of the Crozet Plateau during the austral summer 2004/2005, *Deep Sea Res., Part II*, *54*(18–20), 2020–2044, doi:10.1016/j.dsr2.2007.06.010.

Sheridan, C. C., et al. (2002), Suspended particle organic composition and cycling in surface and midwaters of the equatorial Pacific Ocean, *Deep Sea Res., Part I*, *49*(11), 1983–2008, doi:10.1016/S0967-0637(02)00118-8.

Smetacek, V. S. (1985), Role of sinking diatom life-history cycles: Ecological, evolutionary and geological significance, *Mar. Biol. Berlin*, *84*(3), 239–251, doi:10.1007/BF00392493.

Smetacek, V., et al. (2004), The role of grazing in structuring Southern Ocean pelagic ecosystems and biogeochemical cycles, *Antarct. Sci.*, *16*(4), 541–558, doi:10.1017/S0954102004002317.

Strickland, J. D. H., and T. R. Parsons (1968), Inorganic micronutrients in seawater, in *A Practical Handbook of Seawater Analysis*, edited by J. C. Stevenson, pp. 45–137, Fish. Res. Board of Can., Ottawa.

Takahashi, T., et al. (2002), Global sea-air CO_2 flux based on climatological surface ocean pCO_2, and seasonal biological and temperature effects, *Deep Sea Res., Part II*, *49*(9–10), 1601–1622, doi:10.1016/S0967-0645(02)00003-6.

Takeda, S. (1998), Influence of iron availability on nutrient consumption ratio of diatoms in oceanic waters, *Nature*, *393*(6687), 774–777, doi:10.1038/31674.

Tomas, C. R. (1997), *Identifying Marine Phytoplankton*, 858 pp., Academic, New York.

Tsuda, A., et al. (2003), A mesoscale iron enrichment in the western sub-arctic Pacific induces a large centric diatom bloom, *Science*, *300*, 958–961, doi:10.1126/science.1082000.

Venables, H. J., et al. (2007), Physical conditions controlling the early development of a regular phytoplankton bloom north of the Crozet Plateau, Southern Ocean, described using remotely sensed data, *Deep Sea Res., Part II*, *54*(18–20), 1949–1965, doi:10.1016/j.dsr2.2007.06.014.

Walsh, J. J. (1983), Death in the sea: Enigmatic phytoplankton losses, *Prog. Oceanogr.*, *12*(1), 1–86, doi:10.1016/0079-6611(83)90006-X.

Ward, P., et al. (2007), Plankton community structure south and west of South Georgia (Southern Ocean): Links with production and physical forcing, *Deep Sea Res., Part I*, *54*(11), 1871–1889, doi:10.1016/j.dsr.2007.08.008.

J. Holtvoeth and G. A. Wolff, Department of Earth and Ocean Sciences, University of Liverpool, 4 Brownlow St., Liverpool L69 3GP, UK.

A. E. S. Kemp, R. S. Lampitt, and C. M. Moore, National Oceanography Centre, Southampton, University of Southampton, Waterfront Campus, European Way, Southampton SO14 3ZH, UK.

I. Salter, Laboratoire d'Océanographie Microbienne, Observatoire du Banyuls-sur-mer, Université Pierre et Marie Curie, CNRS-INSU-UMR 7621, Ave. du Fontaulé, Banyuls-sur-mer F-66651, France. (driansalter@gmail.com)